The Planetary Science Journal, 5:224 (21pp), 2024 October https://doi.org/10.3847/PSJ/ad6764

Ice Formation, Exsolution, and Multiphase Equilibria in the Methane–Ethane–Nitrogen System at Titan Surface Conditions

Anna E. Engle[1,2], Jennifer Hanley[1,2], Sugata P. Tan[3], William M. Grundy[1,2], Stephen C. Tegler[1], Gerrick E. Lindberg[4], Jordan K. Steckloff[3,5], Shaelyn M. Raposa[1,2], Cecilia L. Thieberger[1,2], Shyanne Dustrud[4,6], Jessica J. Groven[1,7], and Logan A. Pearce[1,8]
[1] Department of Astronomy and Planetary Science, Northern Arizona University, Flagstaff, AZ 86011, USA
[2] Lowell Observatory, Flagstaff, AZ 86001, USA; aengle@lowell.edu
[3] Planetary Science Institute, Tucson, AZ 85719, USA
[4] Department of Chemistry and Biochemistry, Northern Arizona University, Flagstaff, AZ 86011, USA
[5] University of Texas at Austin, Austin, TX 78705, USA
[6] ATC Materials, Flagstaff, AZ 86001, USA
[7] Washington State University, Spokane, WA 99202, USA
[8] Steward Observatory, University of Arizona, Tucson, AZ 85721, USA

Received 2024 February 24; revised 2024 June 15; accepted 2024 July 15; published 2024 October 9

Abstract

Titan is unique among the icy satellites in that it has a thick atmosphere, stable surficial bodies of liquid, and a precipitation system that promotes interactions between the two. Although Titan's surface conditions are typically assumed to be above the freezing point temperatures of the major constituent species of the climate system (methane, ethane, and nitrogen), conditions may be sufficiently cool across parts of Titan to allow for ice formation alongside known liquid-vapor phases. In this study, we used Raman spectroscopy, visual inspection, and the CRYOCHEM 2.0 equation of state to map the appearance of first ice and to quantify the amount of nitrogen dissolution into liquid in the methane–ethane–nitrogen system along a 1.5 bar isobaric cooling path in the temperature range 80–95 K. This was with the intent of (1) determining the effects nitrogen has on the phase behaviors of the methane–ethane binary system, and (2) establishing the temperatures and ternary mixing ratios needed for ice formation on Titan's surface. We found that ethane-rich mixtures enter a three-phase solid–liquid–vapor equilibrium and are characterized by nitrogen-rich exsolution upon freezing and ice that form at the bottom of the sample. With sufficient methane content, the mixtures cross a univariant four-phase solid–liquid–liquid–vapor boundary, which contributes to a distinct isothermal freezing point profile and ice that forms starting at the liquid–liquid interface. Our results generally agree with findings from previous studies of the methane–ethane–nitrogen system and are intended to add to our current understanding of Titan's geochemical processes.

Unified Astronomy Thesaurus concepts: Titan (2186); Saturnian satellites (1427); Planetary surfaces (2113); Surface ices (2117); Ice formation (2092); Chemical thermodynamics (2236); Surface processes (2116)

1. Introduction

Titan's surface is a diverse and exotic landscape. Its frigid conditions (89–95 K), atmospheric photochemistry, and hydrocarbon-based hydrologic cycle translate to a surface made of water-ice bedrock, organic-rich sands, and liquids composed primarily of methane (CH_4), ethane (C_2H_6), and dissolved atmospheric nitrogen (N_2) (Tomasko et al. 2005; Lunine & Atreya 2008; Hörst 2017; Lopes et al. 2019). The identification of stable bodies of liquid on the satellite's surface has been a point of interest, as it is a shared feature with Earth and is unique to these two solar system bodies.

The most significant source of surface liquids is found in the polar regions in the form of lakes and seas (Stofan et al. 2007). The Cassini-Huygens mission found the north pole to have the greatest abundance of lacustrine features, which are filled with methane-rich liquid and may exceed 100 m in depth (Mastrogiuseppe et al. 2019; Lorenz 2021). Additionally, Ligeia Mare has been periodically decorated with RADAR bright "magic islands" near the shorelines, a possible consequence of waves, nitrogen bubbles, and/or suspended solids (Hofgartner et al. 2014, 2016; Cordier & Liger-Belair 2018). At the same time, the south has only a smattering of filled lakes, with many of them apparently receding and having a higher ethane content than those in the north (Brown et al. 2008; Turtle et al. 2011b; Mastrogiuseppe et al. 2018). Cassini also detected empty lake basins at both poles, with some of them likely being remnants of paleoseas (Hayes et al. 2008, 2011; Birch et al. 2018).

Evidence of rainfall has also been recorded and linked to temporal surface brightening events in four equatorial regions (Turtle et al. 2011c; Barnes et al. 2013). These events coincided with cloud activity and were tracked using the Cassini Visual and Infrared Mapping Spectrometer (VIMS) and Imaging Science Subsystem (ISS) instruments. Generally, the rain-moistened areas darkened, remained in this state for a period of weeks to months, brightened beyond their pre-rainfall surface albedos—perhaps as a consequence of vaporization-driven freezing—and then returned to their original state after about an Earth year. Adding to these events, precipitation has almost certainly played a role in shaping Titan's landscape, especially in forming fluvial and alluvial fans and channels (Lorenz et al. 2008; Radebaugh et al. 2018). The liquid-driven landforms were identified across a large expanse of latitudes and, by applying the principles of terrestrial sedimentology, have been

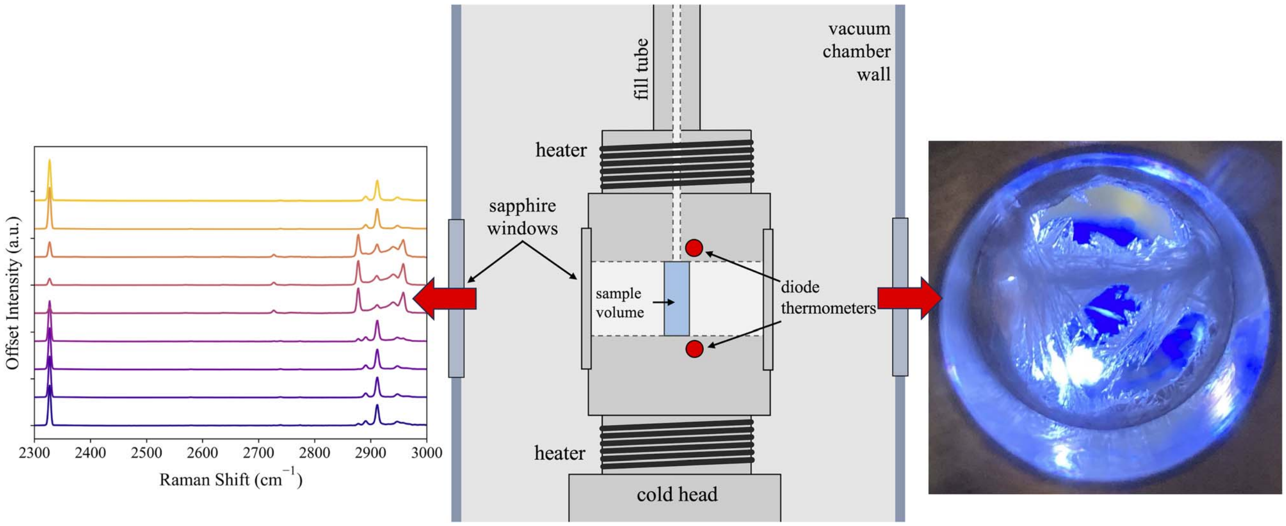

Figure 1. Interior side view of the cell (center) with example outputs from a 0.46 r_M sample. The sapphire windows are positioned on opposite sides of the cell, with one side being used for collecting Raman spectra (left) and the other being used for visual inspection (right). Note: the blue tint in the photo is an attribute of the Raman probe, not a characteristic of the sample.

used to estimate environmental characteristics like sediment transport, relief maturity, and incidents of rainfall.

These liquid-bearing regions contribute to a pattern of surface liquid transience, which is controlled by the hydrologic cycle, operating over seasonal, geologic, and orbital timescales (Hayes et al. 2018; Lora et al. 2022). This corresponds to exchange processes occurring between the atmosphere, surface, and subsurface reservoirs, mainly through means of evaporation and infiltration (Hayes et al. 2011, 2018). The ephemeral nature of the surface liquids has been associated with other surface phenomena captured in the Cassini data, such as “phantom lakes” (MacKenzie et al. 2019), evaporite deposits (Barnes et al. 2011; MacKenzie & Barnes 2016), raised shoreline ramparts (Solomonidou et al. 2020), mudflats (Lopes et al. 2010; Barnes et al. 2014), subsurface access points (Malaska et al. 2022; Wynne et al. 2022), canyons (Poggiali et al. 2016), and the formation of the labyrinth terrain (Malaska et al. 2020).

Several recent computational and experimental studies have shown that adding N_2 to the CH_4–C_2H_6 system perturbs the equilibrium state and has important implications for Titan’s liquids. A key feature of the ternary system is its nonideality, in part due to the difference in miscibility between the three binary systems (i.e., CH_4–C_2H_6, CH_4–N_2, and C_2H_6–N_2). While CH_4 readily mixes with both C_2H_6 and N_2, the same cannot be said for mixtures of C_2H_6 and N_2. As a consequence, the CH_4–C_2H_6–N_2 system can enter a two-liquid equilibrium in which the mixture bifurcates into two stable liquid mixtures simultaneously—characterized by the introduction of a denser N_2-rich bottom layer and a hydrocarbon-rich top layer—when certain combinations of temperature, pressure, and mixing ratio are present (Tan et al. 2015; Cordier et al. 2017; Hanley 2017; Tan & Kargel 2018). And, at certain conditions, the system can also transition into a four-phase solid–liquid–liquid–vapor equilibrium at a quadrupole point (Tan & Kargel 2018; described further in Section 3.3).

As with the changes observed in the phase equilibria, the degree of N_2 dissolution into the system is also affected by temperature, pressure, and mixing ratio. Specifically, higher N_2 solubility is correlated with decreasing temperature, increasing pressure, and increasing CH_4 composition (Malaska et al. 2017; Hartwig et al. 2018; Kumar & Chevrier 2020; Steckloff et al. 2020). Incidentally, N_2 exsolves from the system when warming, creating bubble streams and possibly giving rise to the previously mentioned “magic islands” (Hofgartner et al. 2016; Cordier et al. 2017; Malaska et al. 2017; Farnsworth et al. 2019).

Investigations of the CH_4–C_2H_6–N_2 system under Titan-relevant conditions have provided insight into potential behaviors like suspended ice (Hofgartner & Lunine 2013), floating ethane rain droplets in methane-rich lakes (Farnsworth et al. 2023), lake stratification (Farnsworth et al. 2019; Steckloff et al. 2020), solubility of trace species, the behaviors of cryominerals (Malaska et al. 2011; Malaska & Hodyss 2014; Cable et al. 2021), and generally unique geochemical features (Glein & Shock 2013). These studies have also contributed to determining the feasibility of future missions, such as an autonomous submarine (Richardson et al. 2018, 2019).

Given the ubiquity of the CH_4–C_2H_6–N_2 ternary system on Titan, we conducted a study that probed the effects of N_2 on the CH_4–C_2H_6 system, with the intention of adding to the current body of knowledge. This was achieved by monitoring the phases, phase transitions, and N_2 content of mixtures with N_2-free CH_4 mole fractions (r_M) of 0.0–0.8 r_M at 1.5 bars and 80–95 K. We carried out the experiments in the Astrophysical Materials Laboratory at Northern Arizona University using Raman spectroscopy and visual inspection to map the freezing points of the CH_4–C_2H_6–N_2 system on cooling, record variations in N_2 dissolution and exsolution, and document changes in phase behaviors. The experimental results concerning the freezing points and N_2 content variability were compared to those determined by the CRYOCHEM 2.0 equation of state (EOS; Tan & Kargel 2018). The findings were further compared to the CH_4–C_2H_6 binary liquidus mapped by Engle et al. (2021) to evaluate the impact of N_2 on the alkane system and to elucidate how each of the three binary systems inform freezing point trends.

The implications of this work may be relevant to a number of topics, including the assessment of small-scale shoreline morphology, the propensity for three- and four-phase systems

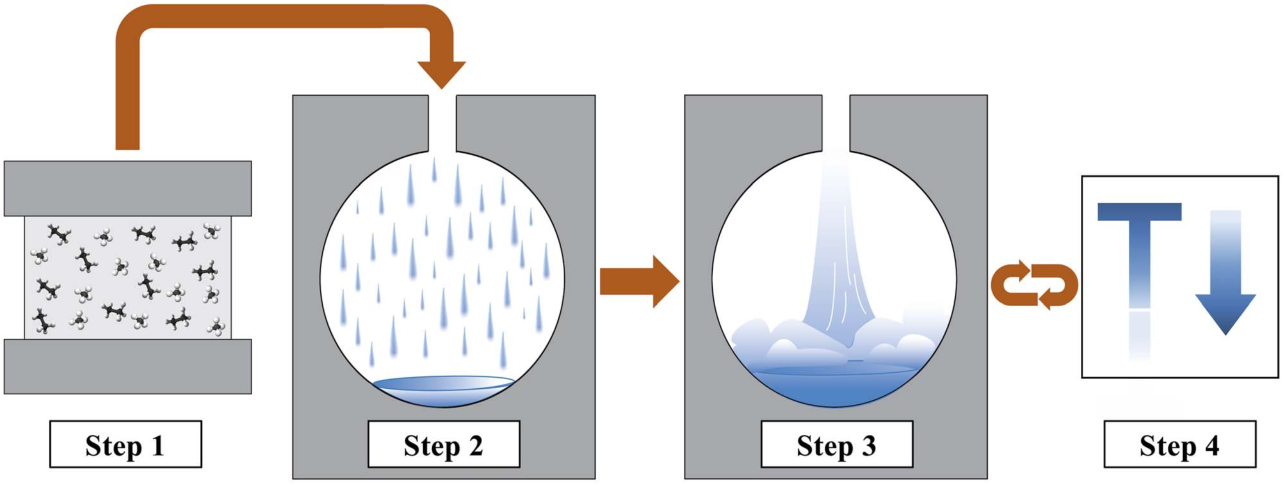

Figure 2. Visual depiction of steps in the experimental protocol. Step 1: the alkane mixture is created in the gas phase in a 0.5-liter mixing chamber. Step 2: the mixture is released into the cell, where it condenses into a liquid. Step 3: nitrogen is injected and used to maintain the 1.5-bar vapor pressure. Step 4: the temperature in the cell is lowered. Steps 3 and 4 are repeated until ice forms or the cell overfills.

to form on Titan, the determination of possible phases and phase transitions in Titan's environment, addressing questions surrounding the satellite's paleo- and future climates, adding insight into evaporative processes, and predicting the conditions needed for cryomineral formation.

2. Methods

2.1. Experimental Setup and Protocol

The experiments were carried out in the Northern Arizona University Astrophysical Materials Laboratory. Mixtures are injected into a cylindrical aluminum alloy sample cell with interior dimensions of 15 mm (diameter) by 5 mm (length). Sapphire windows are forced against indium wire gaskets and allow for visual and spectroscopic inspection of the samples (Figure 1). The cell is cooled from below with a two-stage CTI 1050 closed-cycle helium refrigerator and can reach temperatures as low as 30 K. Diode thermometers and heating elements are mounted on the cell block just above and below the sample volume, which are used to measure and control the temperature and temperature gradient across the sample. The pressure is controlled manually to within ±10 torr (0.01 bars), and a pair of MKS Baratron model 627 F heated capacitance manometers are used to monitor the pressure with a reported precision of ±0.25% of the measured pressure.

We use a Kaiser Rxn1 Raman system equipped with a 785 nm laser and CCD spectrometer to measure Raman shifts over a range of 100–3425 cm^{-1}. The Raman probe, with a 5.5-inch focal length, is mounted on a three-axis stage, allowing us to collect spectra at any location of the cell when multiple phases are present. The spectrometer is set to collect eight scans, which are then summed together to produce the final spectrum. Different exposure times are used depending on the phase(s) in the line of the probe: 3 s for liquid, 15 s for higher scattering solids and solid–liquid mixes, and 30 s for lower scattering solids. This is an important consideration when collecting spectra, as we must strike a balance between good signal-to-noise ratio and avoidance of oversaturation. Further lab descriptions can be found in the literature (e.g., Grundy et al. 2011; Tegler et al. 2019; Engle et al. 2021; Raposa et al. 2022), with the most recent laboratory configuration described by Raposa et al. (2024, in review).

All experiments used in our analysis followed the same protocol (Figure 2). We began with mixing methane (CH_4) and ethane (C_2H_6) in the gas phase in a 0.5-liter mixing volume (Step 1). When the sample cell reached 95 K, the alkane mixture was released from the mixing chamber, where it then rained down and condensed into a liquid (Step 2). Following deposition, we pressurized the cell up to 1.5 bars using gaseous nitrogen (N_2) (Step 3). Once the CH_4, C_2H_6, and N_2 were all present in the sample volume, we incrementally stepped down in temperature, allowing the mixture to settle for 30–35 minutes between each step (Step 4). Steps 3 and 4 were then repeated until ice formed or the cell overfilled, i.e., the N_2 continued dissolving into the liquid(s) until the cell reached capacity, causing the sample to rise into the fill tube. When overfilling occurred, we could not reliably track the vapor pressure at the intended temperature, as the liquid level may have risen above the upper temperature diode and heating coil, thus forming an unknown increase in the temperature gradient. Moreover, given that N_2 dissolution is sensitive to temperature, there may have also been a compositional gradient in the upper portion of the sample.

Overfilling meant that either (1) the mixture necessitated more condensed N_2 than the volume allowed for to equilibrate or (2) the sample reached a composition where the vapor phase was no longer sustainable. Case #1 was typically resolved by repeating the experiment with the same alkane ratio but with a smaller quantity of starting liquid, providing more space for the N_2 to condense into the cell. For Case #2, since the vapor phase was not present, the pressure could not be quantified. This generally occurred after crossing the four-phase solid–liquid–liquid–vapor boundary or in samples with compositions $\geqslant 0.8$ N_2-free CH_4 mole fractions, r_M (details provided in Section 3.3 and Appendix A.4).

As previously demonstrated (Malaska et al. 2017; Farnsworth et al. 2019), N_2 dissolves more readily into the CH_4–C_2H_6 system with decreasing temperature and higher CH_4 composition under isobaric conditions. Thus, more N_2 was injected into the cell in order to maintain a constant pressure during the cooling process. While this means that the mixture as a whole changed in composition throughout the experiment, the alkane ratio remained approximately the same. If a CH_4–C_2H_6–N_2 mixture was warmed, some N_2 and a small quantity of CH_4 exsolved from the liquid. This resulted in a slight change in the alkane ratio and led to a slight shift in the expected amount of N_2 injection when the cooling resumed. While these changes in alkane ratio could be tracked when the compositions were calculated after an experiment, we generally kept to a cooling process to minimize the effect. It should also be noted that a small percentage of the alkane mixture would inevitably get trapped in the fill tube when condensing the material into the cell. The trapped material would be integrated into the liquid once N_2 was injected, meaning that the initial CH_4–C_2H_6 mixture was slightly different in comparison to the alkane ratio after N_2 addition. While these complications did not affect the overall results, they are important to consider when inspecting the data files (provided as part of the Data Availability). Since the N_2 was added separately from the alkane liquid and was used to maintain the pressure in the cell, the system will be referred to as the "CH_4–C_2H_6 +N_2 system" throughout this paper.

2.1.1. Quantifying Sample Compositions

The Raman spectra are used to extract compositions of the liquid in the samples while in the two-phase liquid–vapor (LV) equilibrium. Compositions can occasionally be calculated for samples in the three-phase liquid–liquid–vapor (LLV) equilibrium, but this relies on the two phases being well separated and in contact with the window. This ensures that only one liquid is being probed with the spectrometer, as determining the percentages of each phase in the line of the beam is currently not feasible. The same can be said for instances where both a liquid and a solid are present. Nonetheless, we collect vertical scans of the cell during experiments when multiple phases were present, as we can use them for qualitative analysis. In particular, we can estimate which species is present in each phase by noting changes in the intensities, FWHM, and Raman shifts of the peaks.

To derive compositions, we first calculated the integrated band areas for each species by fitting the 2327 cm^{-1} N_2 peak and a suite of six alkane peaks in the 2850–3000 cm^{-1} region with Voigt profiles. The Voigt profile provides the most accurate representation of liquid spectral lineshapes,blending Gaussian and Lorentzian features, which are typically used to fit solid and vapor peaks, respectively (Bradley 2015).

The 2850–3000 cm^{-1} region is composed of overlapping C–H vibrational modes, with one CH_4 peak at 2905 cm^{-1} and five C_2H_6 peaks at 2880, 2882, 2916, 2938, and 2957 cm^{-1}. Note that the peak centers for the pure species are taken from spectra in the liquid phase and are approximations of their Raman shifts throughout the entire study (Table 1); their positions can shift depending on the mixing ratio and temperature, which in turn provides information on changes in the local environment. An example of this can be seen in Figure 4 of Engle et al. (2021), where the C_2H_6 peak center at 2881 cm^{-1} blueshifts with increasing CH_4 content, likely due to changes in the interactions of the methyl groups. While changes in peak positions are an important consideration when fitting the 2850–3000 cm^{-1} region, this effect does not hinder our ability to extract accurate compositions (Bradley 2015). Fitting the overlapping peaks is a necessary component to extracting the integrated band areas, since (1) the band at 2905 cm^{-1} is the only prominent CH_4 peak in our 100–3425 cm^{-1} spectral range and (2) the summation of the C_2H_6 band areas in this region tends to more accurately describe the sample composition, as opposed to any of the isolated C_2H_6 peaks at lower wavenumbers. Figure 3 provides an example fit for a 0.44 r_M sample.

Table 1
Liquid Phase Vibrational Mode Assignments for Pure CH_4 and C_2H_6 at 95 K and pure N_2 at 70 K

	Nitrogen (N_2)	
ν_1[a]	N≡N stretch	2327 cm^{-1}
	Methane (CH_4)	
ν_1[b]	C–H stretch	2905 cm^{-1}
	Ethane (C_2H_6)	
ν_1[c]	CH_3 stretch	2880 cm^{-1}
ν_5[d]	CH_3 stretch	2882 cm^{-1}
$2\nu_{11}$[c]	CH_3 deform	2916 cm^{-1}
$2\nu_8$[c]	CH_3 deform	2938 cm^{-1}
ν_{10}[c]	CH_3 stretch	2957 cm^{-1}

Notes.
[a] Buchsbaum et al. (1984).
[b] Shimanouchi (1972).
[c] Korppi-Tommola et al. (1990).
[d] Wisnosky et al. (1983).

Once fit, the integrated Raman band areas, R_i, can be used as part of the methodology to determine the mixing ratio (Raposa et al. 2024, submitted). The approach also uses information about each pure species—specifically, integrated band areas ($R_{i(\text{pure})}$), density ($\rho_{i(\text{pure})}$), and molar mass ($\mu_{i(\text{pure})}$)—and assumes that (1) R_i for each species, i, scales with the number of molecules per unit volume, N_i, and (2) the Raman cross section of a molecule, $\sigma_{i(\text{pure})}$, is essentially constant. The latter assumption benefits from the narrow temperature range and constant pressure in our experiments. Large temperature and/or pressure ranges can change the fraction of molecules in excited vibrational states (Pelletier 2003), impacting the widths, profiles, and intensities of the peaks and, in turn, the Raman cross section. We tested the validity of Assumption 2 by calculating and comparing the FWHM of each fitted peak in the 2825–3000 cm^{-1} region of pure propane (C_3H_8) over a range of 85.6–110 K. Propane was selected for this test over methane and ethane because it is the largest species used in our lab and has the lowest melting point of any alkane. When considered as a whole, there was a 0.2% variation in FWHM. The primary equations used to derive the molar abundance of each species (x_i) are

$$x_i = \frac{N_i}{N_i + N_j + N_k + \cdots + N_n}, \tag{1}$$

and N_i is determined using

$$N_i = \left(\frac{R_i}{R_{i(\text{pure})}}\right)\left(\frac{\rho_{i(\text{pure})}}{\mu_{i(\text{pure})}}\right). \tag{2}$$

The values used for $\rho_{i(\text{pure})}$ are for the same temperatures and pressures as those recorded when calculating $R_{i(\text{pure})}$ and were obtained through the National Institute of Standards and Technology (NIST) catalog (see Data Availability for the $\rho_{i(\text{pure})}$, $\mu_{i(\text{pure})}$, and $R_{i(\text{pure})}$ values and their associated

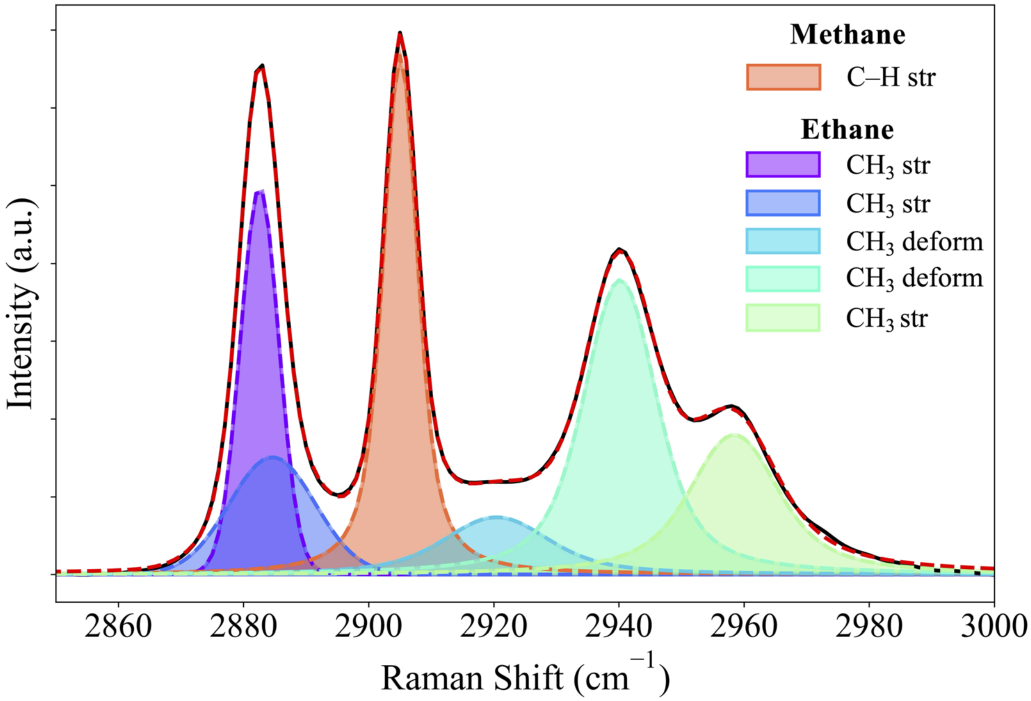

Figure 3. Fitted peaks for quantifying sample compositions using a 0.44 r_M mixture as an example. The 2850–3000 cm^{-1} region is a compilation of overlapping C–H vibrational modes (listed in Table 1).

temperatures and pressures). The experimental R_i and $R_{i(\mathrm{pure})}$ values are used in Equation (2), which is then applied to Equation (1) to get the mole fraction of CH_4, C_2H_6, and N_2 in each mixture. The composition uncertainties were determined to be ±0.03 r_M and account for instrumental effects, spectral noise, results from the Assumption 2 validation experiments, and the precision of the peak fitting.

2.2. CRYOCHEM 2.0

Experiments were compared to calculations produced by the CRYOCHEM 2.0 EOS (Tan et al. 2013; Tan & Kargel 2018). This is an improved version of the original EOS (Tan et al. 2013) and has proven to be reliable in representing multiphase equilibria of multicomponent mixtures at low to moderate pressures and low temperatures. It was used here to model both the freezing point trend and bubble-point curves on isobaric N_2 dissolution and ternary phase diagrams at specific temperatures.

In the following sections, when discussing the results of CRYOCHEM 2.0, phases will be denoted as S for solid, L for liquid, and V for vapor. Subscripted letters will represent dominant species in a given phase: N for nitrogen-rich, M for methane-rich, and E for ethane-rich. Phases with no subscripted letter do not have a dominant species. Interested readers are referred to the original paper cited above for the EOS. A cooling progression of the composition diagrams at 1.5 bars is given in Appendix A.1 to provide further understanding of the freezing detection in our experiments.

As described earlier with the experiments, the isobaric cooling process starts from an LV equilibrium, where the constant pressure is maintained by injecting N_2 as the temperature is lowered. When freezing occurs, the first chunk of solid appears in the presence of vapor, thus in an S_ELV equilibrium. For initial mixtures with substantial amounts of CH_4, the cooling may introduce a second liquid phase that is richer in N_2 prior to the freezing temperature, so that the freezing occurs in four-phase solid–liquid–liquid–vapor (S_ELL_NV) equilibrium.

While two-phase and three-phase equilibria have been much discussed before (Cordier et al. 2017; Tan & Kargel 2018), the four-phase S_ELL_NV equilibrium is a unique state to be modeled in this work. For ternary mixtures, a four-phase equilibrium has 1 degree of freedom, i.e., a univariant system, where only an intensive property is allowed to be freely selected to get all other intensive properties fixed. In the isobaric cooling done for this work, the pressure is selected to be constant at 1.5 bars. Therefore, the S_ELL_NV equilibrium can only happen at a unique temperature that can be calculated by solving the equality of chemical potentials of each species (μ_i) in all phases:

$$\mu_i^S(T, P, \boldsymbol{q}) = \mu_i^{L_N}(T, P, \boldsymbol{w}) = \mu_i^L(T, P, \boldsymbol{x}) \\ = \mu_i^V(T, P, \boldsymbol{y}) \quad i = \mathrm{N, M, N}. \tag{3}$$

With a constant pressure P, the above nine equations (Equation (3)) can solve their nine independent unknowns: the freezing temperature T and the corresponding phase compositions $\boldsymbol{q} = \{q_i\}$, $\boldsymbol{w} = \{w_i\}$, $\boldsymbol{x} = \{x_i\}$, and $\boldsymbol{y} = \{y_i\}$, all with $i = \mathrm{N}$, M. Note that the third species ($i = \mathrm{E}$) is automatically fixed by the fact that mole fractions sum to unity in each phase.

For modeling the dissolution experiments, only two phases are involved, i.e., liquid and vapor, thus in LV equilibrium. Therefore, the equations to solve are the last equations in Equation (3); there are three of them, one for each species. However, these three equations by themselves cannot solve the phase compositions while the temperature and pressure are fixed because there are four unknowns to solve, i.e., x_N, x_M, y_N, and y_M (with the C_2H_6 composition again fixed by these adding to unity). In this case, for general LV equilibrium calculations, the following material balance equation is needed:

$$x_i(1 - v) + y_i v = z_i \quad i = \mathrm{N, M}, \tag{4}$$

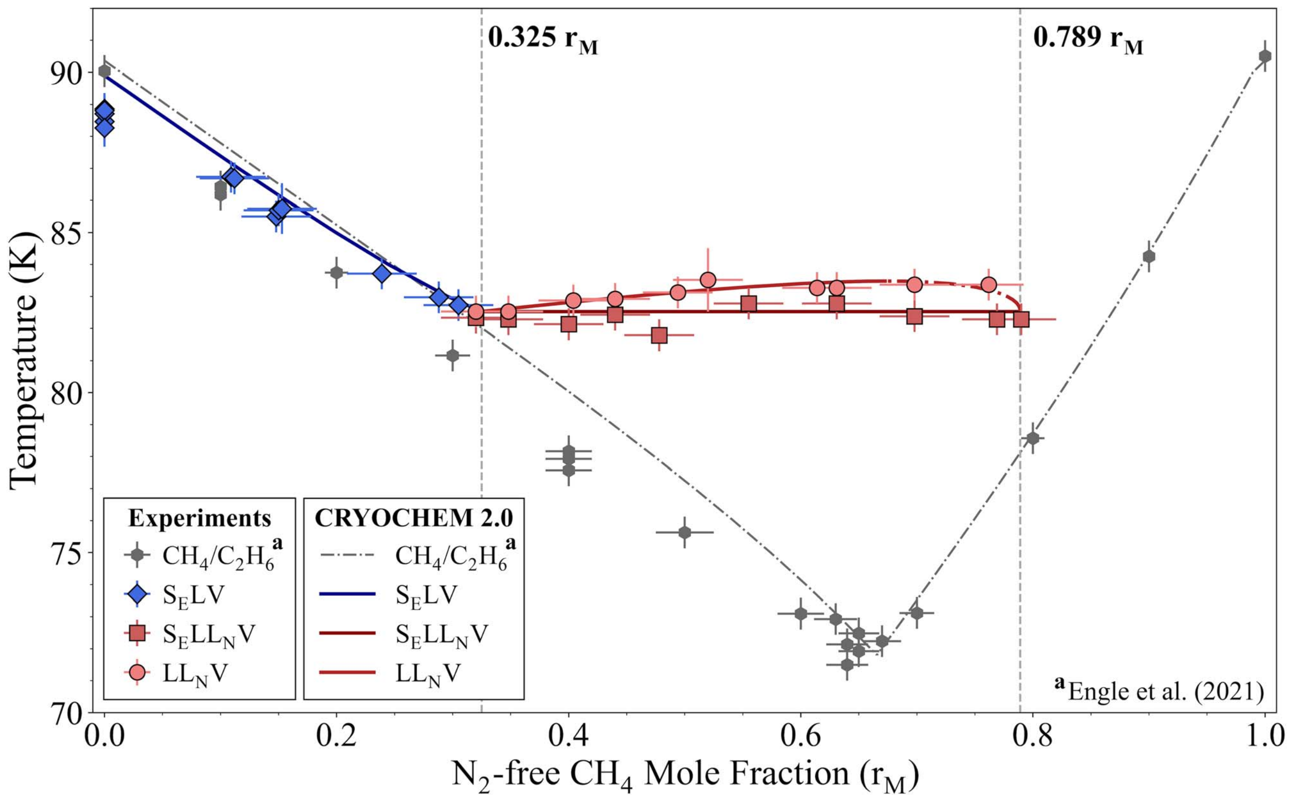

Figure 4. Pseudo-binary phase diagram comparing the freezing points of the CH_4–C_2H_6 $+N_2$ ternary system at 1.5 bars to the liquidus of the CH_4–C_2H_6 binary (Engle et al. 2021). The LL_NV results for the ternary system are also included, with the solid line representing the composition of the L phase and the dashed line denoting the L_N phase. The presence of the vapor phase is removed, showing only the condensed phases. Subscripts: N = nitrogen-rich, M = methane-rich, E = ethane-rich.

where $\boldsymbol{z} = \{z_N, z_M, z_E\}$ is the overall composition of the system that includes all phases, which is usually known in most applications. A new unknown, namely the mole fraction of vapor phase v, is introduced here to be solved together with the phase compositions. Calculating v through Equation (4) is also known as the lever rule.

Note that $\boldsymbol{z}$ is partially known in this work, because only the compositions of the N_2-free alkanes $r_M = z_M/(z_M + z_E)$ are set initially in the mixing cell, but the amount of injected N_2 (thus z_N) is not measured. Therefore, the EOS cannot calculate the liquid composition without applying an additional assumption. Here the measurements are assumed to be made near the bubble point so that approximations can be calculated without the material balance Equation (4) by setting $\boldsymbol{x} = \boldsymbol{z}$ in the last equations of Equation (3) for the LV equilibrium, where three equations can now solve three unknowns (x_N, y_N, and y_M). These approximations are still useful for evaluating the trends of experimental data, as well as giving the limiting values for the data to compare with. All EOS parameters used in this work are taken from those used in Tan & Kargel (2018), except for the solid binary interaction parameter of CH_4–C_2H_6, which is adjusted from 0.06 to 0.075 to get a better fit to the measured eutectic temperature.

3. Results

Figure 4 depicts the impact N_2 has on the CH_4–C_2H_6 system (Engle et al. 2021). The results of the ternary mixtures represent where the ice was detected for the first time along the 1.5-bar isobaric cooling path. Note that it was the vapor phase that provided the pressure; thus, the results indicate when freezing occurred while in the presence of the vapor phase. Essentially, the diagram overlays the three-dimensional projection of the ternary results onto the two-dimensional binary phase diagram. This formatting will be referred to as a “pseudo-binary phase diagram,” as the ternary projection extends beyond the technical definition of a standard binary phase diagram. The format is intended to emphasize the deviation of the ternary mixtures from that of the alkane system and so is reported in CH_4 N_2-free mole fraction, r_M. Since Figure 4 only provides information in relation to the CH_4–C_2H_6 ratios, we also built complementary isobaric ternary phase diagrams for each r_M considered (e.g., Figure 5). The diagrams track N_2 dissolution along a line of constant r_M (referred to as the $+N_2$ cooling path) while in LV equilibrium and as temperature is lowered.

The diagram in Figure 4 is divided into two distinct solid-bearing regions that are classified by the phase boundaries crossed when ice first appears along the $+N_2$ cooling path. Beyond ~0.8 r_M, the freezing point profile ceases because ice cannot form while in the presence of the vapor phase on the $+N_2$ isobaric cooling path. The following sections provide details on the results of the multiphase equilibria. Section 3.1 focuses on N_2 dissolution into the LV equilibrium prior to freezing, Section 3.2 describes the behavior of the system when crossing the S_ELV boundary, and Section 3.3 provides the same context as Section 3.2 but for the case of the LL_NV and S_ELL_NV boundaries. Further information is also given on the part of the diagram with >0.8 r_M in Section 3.3 and Appendix A.4. Lastly, Section 3.4 showcases the variations in ice morphology of the ternary system along the freezing point profile depicted in Figure 4.

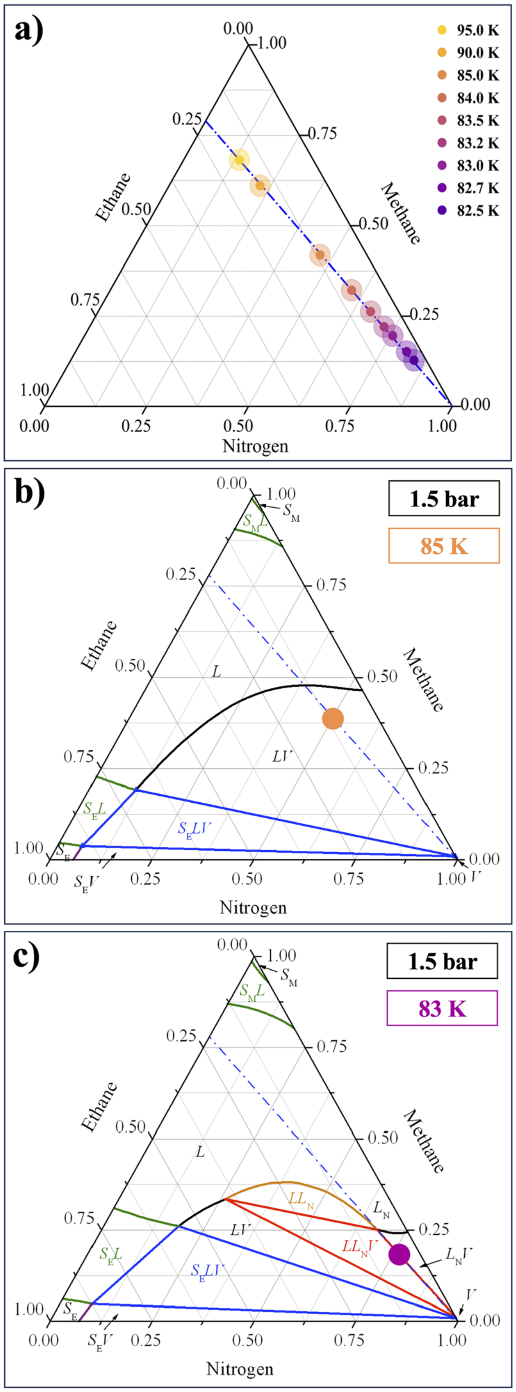

Figure 5. Using ternary diagrams to track N_2 addition into a 0.79 r_M sample. (a) An isobaric diagram showing the increasing N_2 content with decreasing temperature along a constant r_M line in an experiment. (b, c) Examples of isobaric ternary diagrams at 1.5 bars produced by CRYOCHEM 2.0 and marking the phase equilibria and compositions of the sample at 85 and 83 K, respectively.

3.1. Nitrogen Dissolution into the LV Equilibrium

Experimental work performed by Malaska et al. (2017) demonstrated that N_2 dissolution into the ternary system generally increases with decreasing temperature, increasing CH_4 composition, and increasing pressure. Our results concerning N_2 dissolution into samples at LV equilibrium reflect the same trends for temperature and CH_4 composition (Figure 6); we cannot comment on the relationship between N_2 dissolution and pressure, given that our study was conducted at isobaric conditions. Note that the results collected in the Astrophysical Materials Lab are confined to the LV equilibrium, meaning that there are no experimental data points in Figure 6 that pertain to the LLV, SLV, or SLL equilibria. In other words, no data points should lie at temperatures lower than the LLV or SLV three-phase boundaries, where the N_2-rich liquid L_N or C_2H_6-rich solid S_E appears, respectively. Noticeably, the experimental values in Figure 6 show higher quantities of N_2 dissolution as compared to the model. This is likely due to a combination of the uncertainties associated with the composition derivation protocol (± 0.03 r_M) and the relatively small increases in N_2 content while traveling along the $+N_2$ cooling path.

Interestingly, the spectra collected for samples in LV equilibrium exhibit trends that correlate with the S_ELV and S_ELL_NV regions delineated in Figure 4. Experimental samples with compositions <0.32 r_M are associated with the S_ELV region, and spectra for a 0.29 r_M sample (Figure 7) illustrate the shared spectral characteristics. Namely, the increase in intensity of the N_2 peak at 2327 cm^{-1} along the cooling path is minimal, and the peak centers noted in Figures 7(b) and 8(c) with vertical dotted lines shift by $\leqslant 1$ cm^{-1}. Together, these traits indicate low N_2 content and solubility, as well as little disruption to the molecular environment. This is in contrast to the behavior descriptive of the S_ELL_NV region, which spans compositions of 0.32–0.79 r_M and is shown through the spectra of a 0.79 r_M sample (Figure 8). Here the intensity of the N_2 peak increases substantially with decreasing temperature, which is especially prominent at low temperatures where the temperature step was reduced to 0.2–0.3 K. Additionally, the N_2 peak at 2325 cm^{-1} blueshifts by 1.5 cm^{-1} (Figure 8(b)), the C_2H_6 peak at 2886 cm^{-1} blueshifts by 4 cm^{-1}, and the CH_4 peak at 2905 cm^{-1} blueshifts by 5 cm^{-1} (Figure 8(c)) when cooling from 95 K down to 82.5 K. Unlike the S_ELV compositions, this implies an evolving system, with a notable deviation being in the shifting of the CH_4 peak. We find that the CH_4 peak center remains relatively stable at 2904 cm^{-1} in both the CH_4–C_2H_6 binary system and ternary mixtures associated with the S_ELV region, regardless of changes in temperature or composition. Given that the composition progresses from 0.14 N_2 at 95 K to 0.84 N_2 at 82.5 K, the peak shift could be a consequence of N_2 becoming the more common nearest neighbor to CH_4 and thus intervening on the interactions between the two alkanes.

Figure 9 shows the isobaric composition diagrams at 90 and 95 K, where the two-phase LV equilibrium is dominant. The solid phases first appear on the diagram at about 90 K in the vicinity of pure CH_4 and C_2H_6, as it is very close to their triple points. As seen in the figure, all data follow the trend given by the liquid boundaries, which are the bubble-point curves calculated as described in the previous section. The trend of N_2 dissolution increasing with lower temperature and increasing r_M is nonlinear below the freezing points of CH_4 ($\sim$91 K) and C_2H_6 ($\sim$90 K), demonstrating that previous (e.g., Hartwig et al. 2018) and future models will need to account for this effect. Some other representative ternary diagrams at lower temperatures are provided in Appendix A.3.

3.2. Crossing the Three-phase S_ELV Boundary

At 1.5 bars, mixtures with $\leqslant 0.32 \pm 0.03$ r_M experimentally and $\leqslant 0.325$ r_M computationally cross the three-phase S_ELV

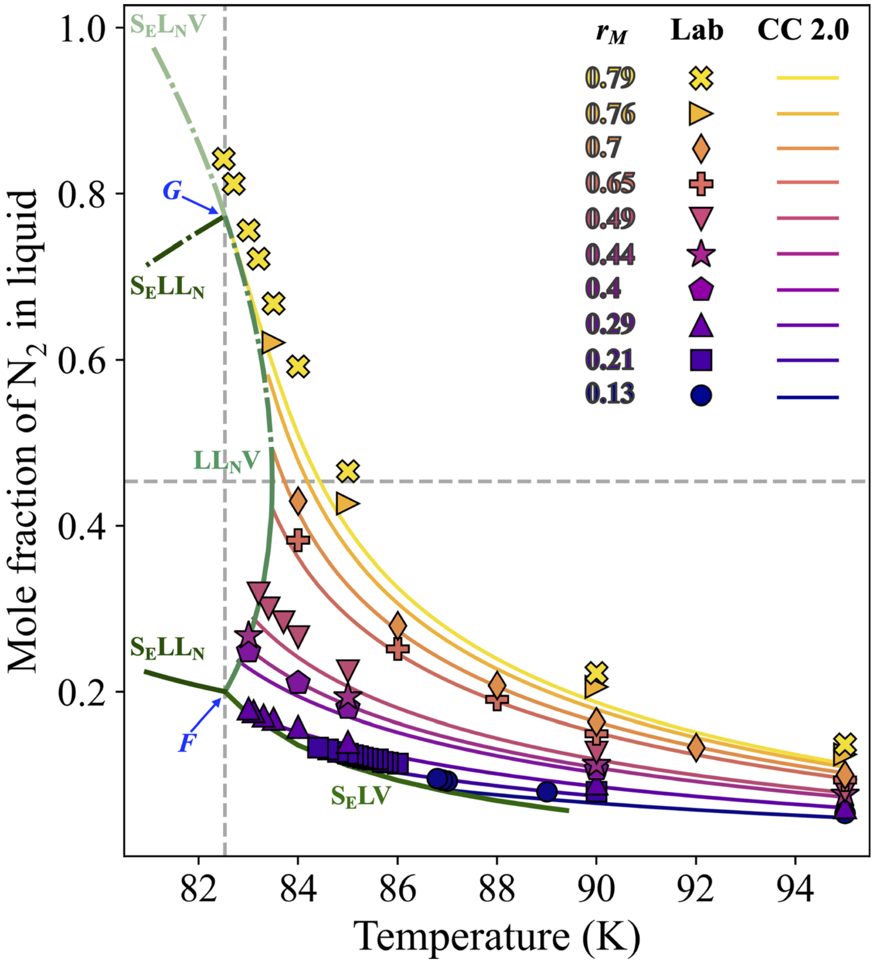

Figure 6. N_2 dissolution into the LV equilibrium system as a function of temperature. The greater the CH_4 N_2-free mole fraction (r_M) and the lower the temperature, the more N_2 dissolves into the system. Experimental data are presented with uncertainties ±0.03 N_2 and ±0.5 K. The bubble-point curves and three-phase LL_NV, S_ELV, S_ELL_N, and SL_NV boundaries are the results from CRYOCHEM 2.0 (CC 2.0) calculations. Points F and G are in the four-phase S_ELL_NV equilibrium at 82.53 K and connected by the vertical dashed line. The horizontal dashed line delineates liquid composition; liquid above the line is N_2-rich (L_N), while liquid below it does not have a dominant species (L).

boundary when ice forms. In this region of the diagram (Figure 4), the ternary compositions are C_2H_6-rich and the freezing point trend is notably similar to the C_2H_6 branch of the CH_4–C_2H_6 binary system liquidus, likely due to the low N_2 solubility into the alkane liquid. According to the model, adding N_2 lowers the freezing point temperatures in comparison to the binary system at compositions <0.325 r_M. For ternary mixtures with compositions in a range of 0.325–0.789 r_M, the freezing point temperature remains constant because of the onset of a four-phase S_ELL_NV equilibrium as a second liquid L_N appears prior to freezing, which is not observed in the binary system. As described in Section 2.2, a four-phase equilibrium of a ternary mixture is univariant, so that there is only a temperature for a fixed pressure. In this case, it is calculated through Equation (3) to be 82.53 K at 1.5 bars, compared to 82.3 ± 0.5 K experimentally. This equilibrium is discussed further in Section 3.3.

As is evident in Figure 4, the experimental temperatures for the CH_4–C_2H_6 liquidus are slightly offset as compared to those determined by CRYOCHEM 2.0, whereas the freezing points for the CH_4–C_2H_6 $+N_2$ system are generally in agreement with the model. Previous work on the CH_4–C_2H_6 binary system in the Astrophysical Materials Lab (Engle et al. 2021) attributed the discrepancy to a supercooling effect induced by the plasticity of C_2H_6 phase I. The study used a settling time (t_{settling}) of 20 minutes when collecting the liquidus data, whereas we opted for $t_{\mathrm{settling}} = 30$–35 minutes for the CH_4–C_2H_6 $+N_2$ experiments, which was chosen because of the supercooling in the binary system. While the increased t_{settling} appears to have subdued the effect, we did find that the supercooling persisted into this region of the CH_4–C_2H_6 $+N_2$ system and is likely due to the high quantity of C_2H_6 in the affected mixtures. Preliminary experiments where $t_{\mathrm{settling}} = 10$–20 minutes provide additional evidence, as the resulting freezing point temperatures were generally lower than those recorded with $t_{\mathrm{settling}} = 30$–35 minutes. Spectra also indicated that C_2H_6 transitioned directly from liquid to solid phase III, which is characteristic of the supercooling effect reported in the binary system. However, the supercooling seems to be negligible at the S_ELL_NV equilibrium, due to their univariant nature.

Focusing in on the C_2H_6 $+N_2$ results, samples that had $t_{\mathrm{settling}} = 30$–35 minutes froze at 88.6 ± 0.6 K, whereas CRYOCHEM 2.0 determined a freezing point temperature of 89.9 K. A similar study performed by Singh et al. (2017a) reported freezing in a range of 87–90 K, which agrees with both our experimental and modeling results. It may be that Singh et al. (2017a) also experienced C_2H_6 supercooling but to varying

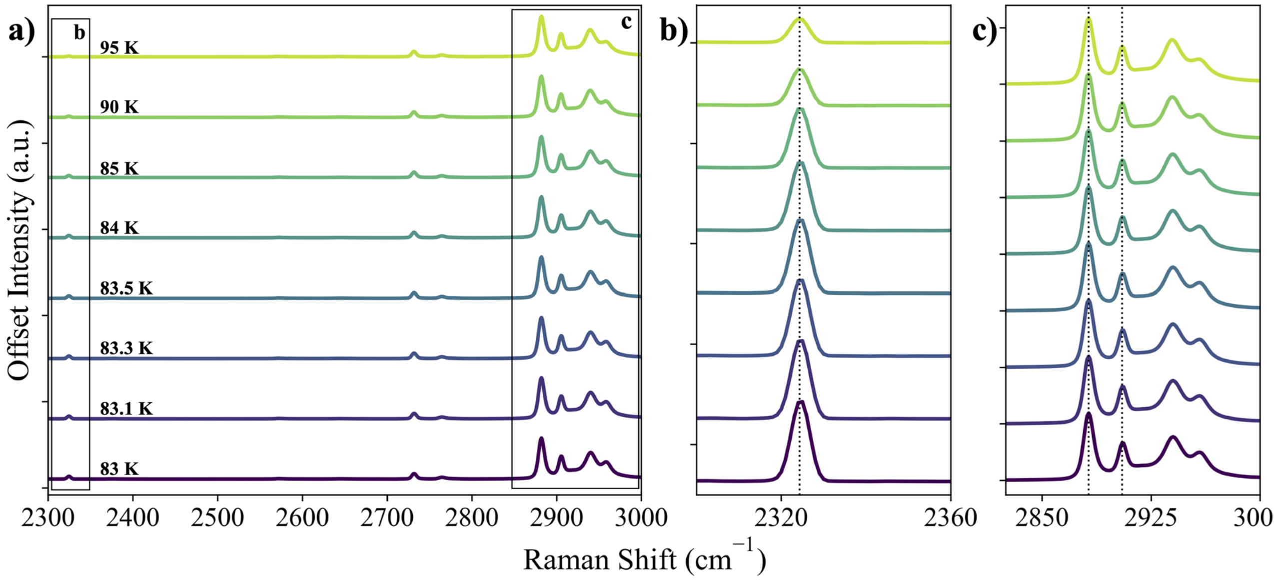

Figure 7. Raman spectra associated with the 0.29 r_M results in Figure 6, which is a composition that is representative of the behavior in the S_ELV region of the pseudo-binary phase diagram. Panel (a) shows the spectral range used for deriving compositions (2300–3000 cm^{-1}) from starting at 95 K and traveling down the $+N_2$ cooling path to 83 K. Panels (b) and (c) are zoomed-in regions of the N_2 peak and CH_4/C_2H_6 peaks, respectively. The dotted lines mark the peak centers at 95 K and show that there is minimal shifting despite decreasing temperature and increasing N_2 content.

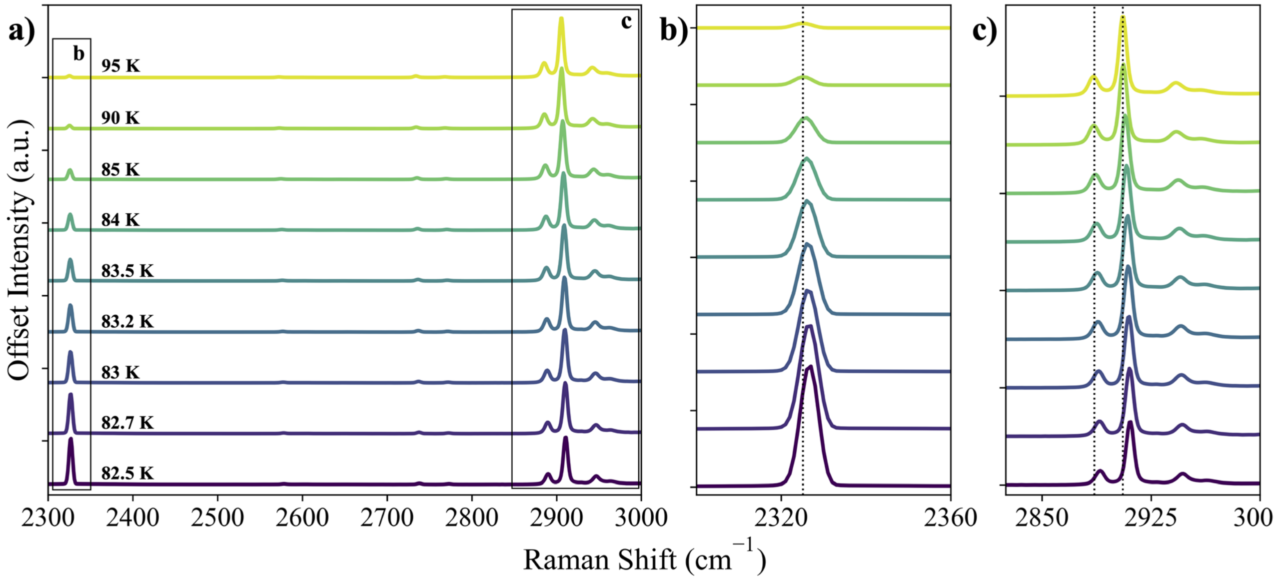

Figure 8. Raman spectra associated with the 0.79 r_M results in Figure 6, which is a composition that is representative of the behavior in the S_ELV_NV region of the pseudo-binary phase diagram. Panel (a) shows the spectral range used for deriving compositions (2300–3000 cm^{-1}) from starting at 95 K and traveling down the $+N_2$ cooling path to 82.5 K. Panels (b) and (c) are zoomed-in regions of the N_2 peak and CH_4/C_2H_6 peaks, respectively. The dotted lines mark the peak centers at 95 K, and, unlike the spectra in the 0.29 r_M sample, all three noted peaks blueshift with decreasing temperature and increasing N_2 content.

degrees. Focused studies on the correlation between sample settling time and freezing point temperature in C_2H_6-rich mixtures would be an important addition to this work, and this could have its own implications for Titan.

3.2.1. *Exsolution at the First Appearance of Ice*

Although low N_2 miscibility into C_2H_6-rich liquids resulted in similar trends between the ternary and binary systems, it was also the instigator for nonideal behaviors, e.g., N_2 exsolution at the onset of ice. The exsolution was most apparent in C_2H_6 $+N_2$ mixtures, where both pressure spikes and changes in spectral features indicated N_2 escaping as C_2H_6 froze (Figure 10). In particular, the N_2 peak at approximately 2327 cm^{-1} becomes undetectable at 88 K in Figure 10 and coincides with redshifting, narrowing, and intensity fluctuations of peaks associated with the liquid → solid transition in C_2H_6 (2730 cm^{-1}, 2765 cm^{-1}, and those listed in Table 1). The process also prompted the formation of small-scale icy domes (referred to here as a "cryodome") at the meniscus (Figure 11; see Data Availability for example time lapse), which were caused by trapped N_2 percolating through the C_2H_6-rich slurry, building and solidifying as the vapor escaped.

We were unable to identify a single variable responsible for the size and scale of the cryodomes, although factors like temperature step (T_{step}), settling time between temperature

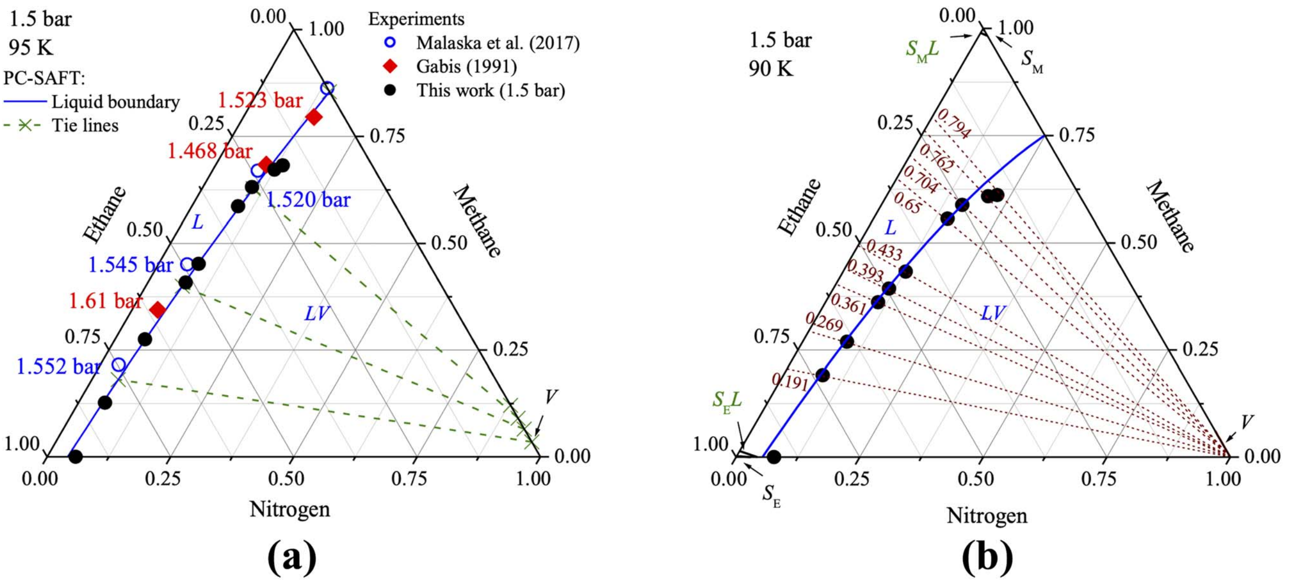

Figure 9. The ternary CH_4–C_2H_6 + N_2 composition phase diagrams at 1.5 bars and at (a) 95 K and (b) 90 K. The black filled circles are the measured data from this work, with compositional uncertainties of ± 0.03 r_M. The blue open circles and red filled diamonds are from the literature. Green dashed lines at 95 K are typical tie lines connecting equilibrium compositions in liquid and vapor. Brown dotted lines at 90 K are the $+N_2$ cooling paths (constant r_M as indicated on each of the lines).

steps (t_{settling}), and sample volume appear to have contributed to the end product. It is also possible that viscosity and initial pressure contributed to variations in mini-cryodome formation, although these have not been well tested. Figure 11 provides visuals of the primary morphologies seen during these events; they are (a) one larger cryodome, (b) multiple smaller cryodomes, (c) flat/expanded, and (d) flat/undisturbed. The sample images are accompanied by their respective values for the temperature-related factors.

While the effects were most prominent in C_2H_6–N_2 mixtures, N_2 exsolution persisted throughout the S_ELV region and ceased once in the S_ELL_NV region. Generally, we found that as r_M increased, both the freezing point temperature and the quantity of N_2 exsolution decreased. This was likely due to an increase in CH_4-rich liquid residing in the cell after ice formation since a majority of the C_2H_6 transitioned to the solid phase. As a consequence of lower exsolution rates, the pressure spike witnessed at the onset of ice also decreased with increasing CH_4 content.

We detected no apparent cryodome formation in the ternary mixtures, but time lapses indicate that bubbling still occurred. Since the laboratory setup only allows for a side view of the sample, we could not fully determine whether the process promoted any surface roughening, although the continued presence of percolation suggests that there may have been slight undulations after the meniscus solidified. The combination of exsolution and a lack of observable cryodome formation bears some resemblance to a study by Farnsworth et al. (2019). Namely, they reported N_2 bubbles being impeded by a layer of ice likely composed of C_2H_6; no signs of surface roughening were reported. Given that their experiments were performed with mixtures of all three species, this result is in line with our observations.

3.3. Crossing the Four-phase S_ELL_NV Boundary

The flat profile on the pseudo-binary phase diagram (Figure 4) shows the occurrence of a four-phase solid–liquid–liquid–vapor (S_ELL_NV) equilibrium at 1.5 bars. According to the phase rule, four-phase equilibria are univariant, meaning that they can only occur at a specific temperature for a fixed pressure. At 1.5 bars, CRYOCHEM 2.0 determined that the four-phase boundary forms at 82.53 K, serving as a freezing point in a composition range of 0.325–0.789 r_M, with experiments indicating formation at 82.3 ± 0.5 K in a range of 0.32 ± 0.03 r_M and 0.79 ± 0.03 r_M. The isothermal temperature profile is in sharp contrast to the CH_4–C_2H_6 binary system, where the liquidus reaches a eutectic point of 0.675 CH_4 at 72.6 K computationally and 0.64 ± 0.02 CH_4 at 72.2 ± 0.4 K experimentally (Engle et al. 2021).

The S_ELL_NV equilibrium is an inevitable feature of the CH_4–C_2H_6–N_2 system and is due to the formation of a N_2-rich liquid, leading to an LL_NV equilibrium prior to freezing along the $+N_2$ cooling path (Figure 4). While all three species are present in the two liquids, C_2H_6 tends to be mostly sequestered to the upper layer, N_2 is predominantly found in the lower layer, and CH_4 is dispersed between the two, although with a slight inclination toward residing in the upper layer. Since the N_2-rich liquid is denser and is consistently added to maintain constant vapor pressure, the newly forming phase will first condense at the meniscus, creating a droplet that eventually falls to the bottom of the cell. The delineation between the two liquids is evidenced not only from visual inspection (Figure 12) but through spectral variations as well.

Once the second liquid begins to form, N_2 readily dissolves into the system and continues to do so even after ice has formed. The behavior differs from the S_ELV region, where the notable trait is N_2 exsolution at the onset of ice. Mixtures with 0.29–0.76 r_M will cross the calculated three-phase LL_NV boundary at approximately 82.53–83.48 K, while <0.29 r_M mixtures will cross the three-phase S_ELV at temperatures above 82.53 K, and >0.76 r_M mixtures will cross the three-phase S_EL_NV below 82.53 K (Figure 6). At 82.53 K, the S_ELV and S_EL_NV boundaries merge with LL_NV to the S_ELL_NV equilibrium at points F and G in Figure 6, which are unique to the CH_4–C_2H_6 $+N_2$ system at 1.5 bars. Thus, ice first appears at the same temperature and results in the isothermal profile seen in Figure 4. In the S_ELL_NV equilibrium, the

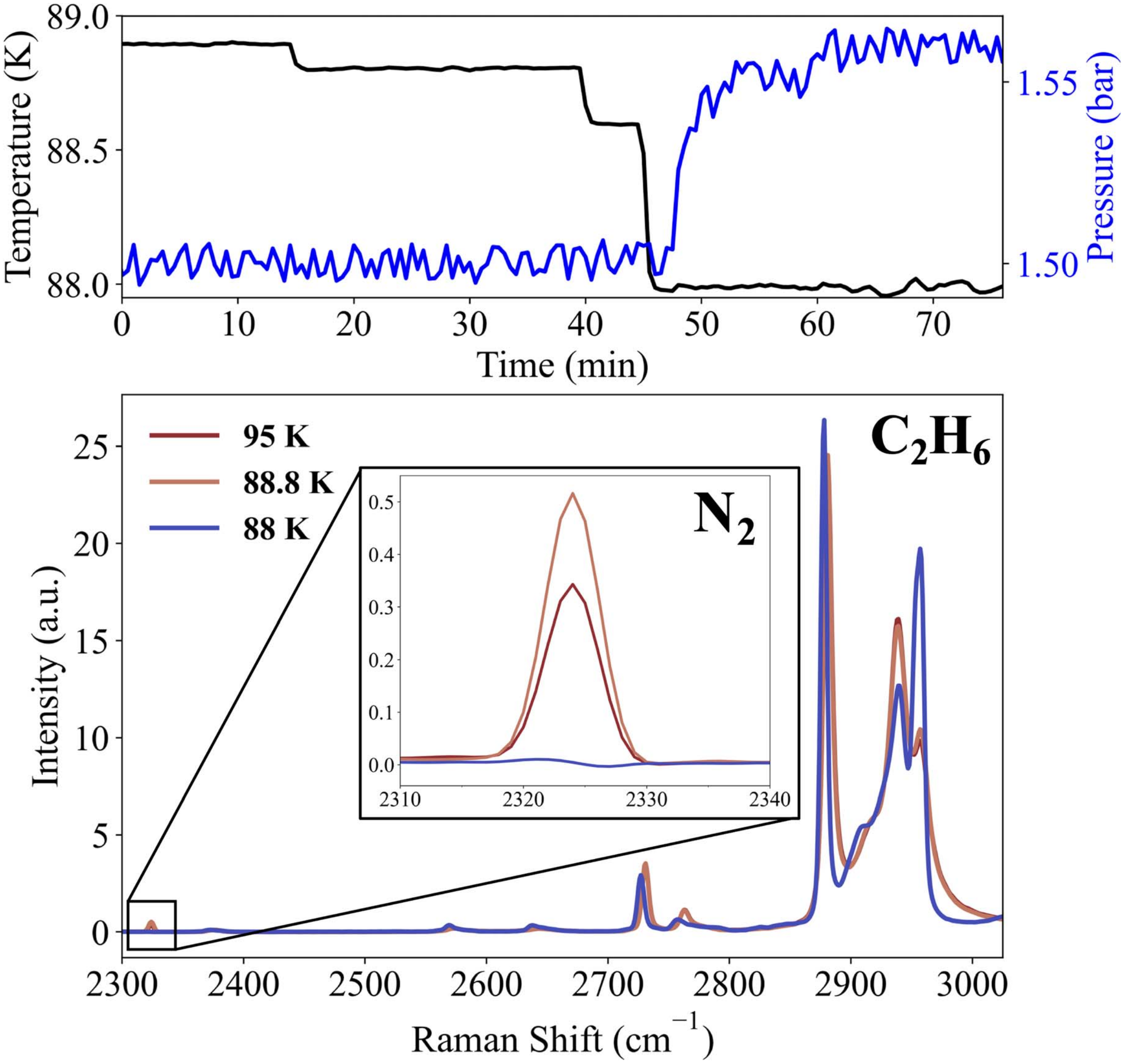

Figure 10. Evidence of N_2 exsolution from a $C_2H_6 + N_2$ sample. Top: the vapor pressure rose in the cell shortly after the temperature was lowered to 88 K, which incited freezing. Bottom: normalized Raman spectra of the sample pre- and post-freezing, shown in red and blue, respectively. The inset demonstrates a complete exsolution of N_2, while the peaks between 2850 and 3000 cm^{-1} indicate that all, or nearly all, of the C_2H_6 solidified.

compositions of the liquids are fixed, calculated to be ($0.260\ CH_4/0.540\ C_2H_6/0.200\ N_2$) and ($0.179\ CH_4/0.048\ C_2H_6/0.773\ N_2$), plotted as small white triangles in Figure 13, which are at 0.325 r_M and 0.789 r_M, respectively, and correspond to points F and G in Figure 6. On further cooling, the four-phase region splits once again into two three-phase regions but with differing combinations than those seen prior to crossing the S_ELL_NV boundary (i.e., S_ELL_N and S_EL_NV) as described in Appendix A.4.

Since the four-phase equilibrium is univariant and the sample cell has a slight temperature gradient, we are unable to stabilize a sample at the precise pressure–temperature combination. However, we can visually capture the changes that occur in a sample as a consequence of crossing the S_ELL_NV boundary (e.g., Figure 14(d)). A time lapse of the progression is provided in Data Availability.

As is detailed in Section 2.1, this study followed a protocol where the alkanes were condensed as a liquid and N_2 was then incrementally injected to maintain the vapor pressure. CRYOCHEM 2.0 shows in Figure 13 that, for this format, mixtures with >0.79 r_M miss the four-phase equilibrium and thus cannot form ice while in the presence of a vapor phase. Technically, freezing could occur at 82 K (see Appendix A.4), but it is not attainable along the $+N_2$ cooling path because it cannot reach the L_NV region. Therefore, it will not be able to maintain a vapor phase prior to crossing the S_EL_NV region. However, ice formation may be possible by adjusting the protocol, so a CH_4–N_2 mixture is condensed as the liquid and the line of constant r_M is along a $+C_2H_6$ cooling path. Although this procedure is experimentally feasible in our lab, it is beyond the intent of this study and is not considered here. Regardless of the cooling path orientation, no ice will form while in the presence of vapor at ⩽81 K, as this is the condensation point of N_2 at 1.5 bars.

3.4. Ice Morphology in the CH_4–C_2H_6 $+N_2$ System

The crystal morphologies in the CH_4–C_2H_6 $+N_2$ samples share common characteristics based on whether they are in S_ELV (Figures 14(a)–(c)), S_ELL_NV (Figure 14(d)), or S_EL_NV equilibrium (Figures 14(e)–(f)). A previous study of the

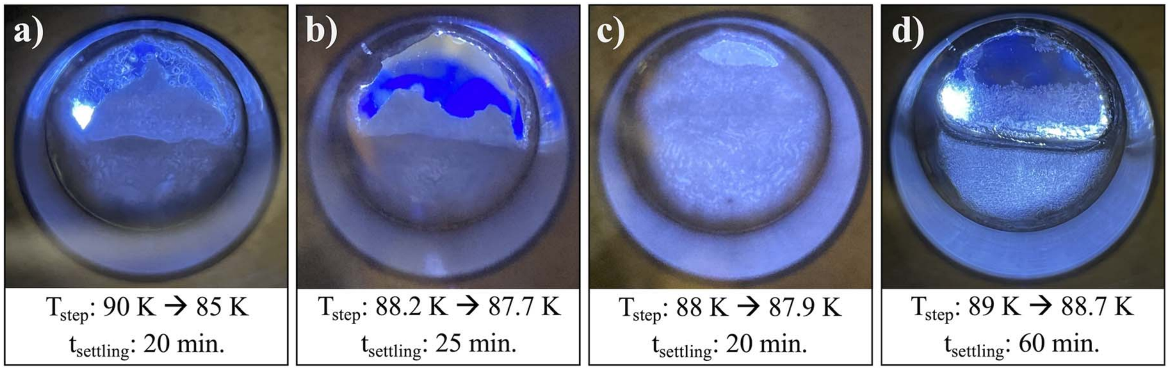

a) T_{step}: 90 K → 85 K; $t_{settling}$: 20 min.
b) T_{step}: 88.2 K → 87.7 K; $t_{settling}$: 25 min.
c) T_{step}: 88 K → 87.9 K; $t_{settling}$: 20 min.
d) T_{step}: 89 K → 88.7 K; $t_{settling}$: 60 min.

Figure 11. Effects of N_2 exsolution on ice morphology in four different C_2H_6 +N_2 samples. The primary formations seen during experiments were (a) one larger cryodome, (b) multiple smaller cryodomes, (c) flat/expanded, and (d) flat/undisturbed. T_{step} indicates the temperature step during which ice formed, and $t_{settling}$ is the amount of time the sample was allowed to settle between each temperature step previous to ice formation.

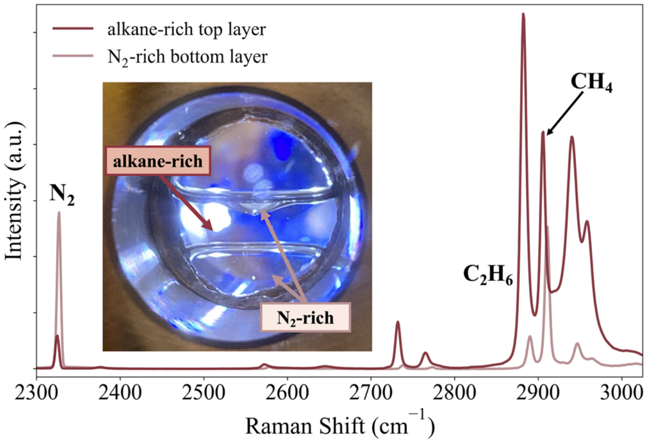

Figure 12. Example of LL_NV equilibrium in a 0.40 r_M sample at 82.3 K. All three species are present in both liquids and spectra indicate that C_2H_6 is mostly found in the top layer, N_2 in the bottom layer, and CH_4 dispersed between the two.

CH_4–C_2H_6 binary system in the Astrophysical Materials Lab showed that C_2H_6-rich ice forms at the bottom of the cell in mixtures along the C_2H_6 branch of the liquidus and CH_4-rich ice forms at the meniscus in mixtures on the CH_4 branch (Engle et al. 2021). Texturally, the C_2H_6-rich ice is needle-like, whereas the CH_4-rich ice tends to be less defined. Comparatively, the ice in the S_ELV region behaves similarly to the C_2H_6-rich alkane mixtures in that it forms at or near the bottom of the cell and expands upward. However, the morphology is more dendritic or "feathery," as opposed to the needle-like structure seen in the binary system, and as r_M increases, the ice becomes more tenuous (Figures 14(a)–(c)), which is likely due to the increased retention of N_2 in the liquid phase. In the S_ELL_NV region, the ice takes on a "spiky" quality. On cooling, these mixtures first enter an LL_NV equilibrium, splitting into a N_2-rich (L_N) bottom layer and a hydrocarbon-rich (L) top layer. Cooling further, C_2H_6-rich ice forms in the hydrocarbon-rich layer, generally starting at the LL_N interface (clearly exemplified in Figure 14(d)) and expands throughout the L layer as the sample crosses the S_ELL_NV boundary (e.g., Figure 14(e)). The volume of the N_2-rich layer continues to increase with increasing r_M, and at ~0.8 r_M, the liquid phase separation is barely present, completely disappearing in mixtures exceeding 0.8 r_M. As the L layer recedes, the quantity and morphology of the ice change, and the progression can be seen in Figures 14(d)–(f).

CRYOCHEM 2.0 can be used to calculate the density of each phase in a given system. Although we cannot quantitatively measure densities for our samples, we are able to qualitatively compare the laboratory results with those determined by the EOS. Overall, we found that the locations where ice formed in the cell agreed with the model. The calculations projected that S_E would sink in L above the four-phase temperature and float in L_N below it. Visuals of this are depicted in Figure 14, and the calculated densities at the S_ELL_NV equilibrium can be found in Table A1.

4. Discussion and Implications

At face value, it is unlikely that ice can form where liquids reside on Titan's surface. The northern lakes in particular lack the possibility given their projected compositional values of 0.35–0.70 r_M (or 0.54–0.80 $CH_4/(CH_4+C_2H_6+N_2)$ content; Mastrogiuseppe et al. 2019), falling within the S_ELL_NV region in Figure 4 and thus uniformly correlating to a freezing point of about 82.5 K. According to our results, at recorded Titan surface temperatures (89–95 K) the liquid in the lakes would have to be $\leqslant 0.05$ r_M for ice to form, which is not a feasible scenario, especially at the poles, where the lower temperatures are more conducive to CH_4-rich liquids condensing onto the surface (Tan et al. 2015). Further, this assumption is compounded with studies suggesting minimal contrast between the surface temperatures of the lakes and land (Jennings et al. 2016; Le Gall et al. 2016). Nonetheless, the existence of ice near liquid reservoirs, past or present, should not be fully discounted. Such scenarios would necessitate processes that could lower surface temperatures and/or increase C_2H_6 content. This may include areas of shallow liquids like shorelines, puddles, and wetlands; changes in the behavior and evolution of cold rain as it falls and flows across the surface; and a snowball/slushball Titan paleoclimate.

4.1. Exsolution in the Presence of C_2H_6-rich Ice

In line with previous studies, we found only small quantities of N_2 dissolved into C_2H_6-rich liquids and that it exsolved when the sample was warmed. Interestingly, we also recorded N_2 exsolution at the onset of ice, which, to the best of our knowledge, has not been reported in the literature. Farnsworth et al. (2019) recorded the closest outcome, witnessing N_2 bubbles being obstructed by a "cap" of C_2H_6-rich ice.

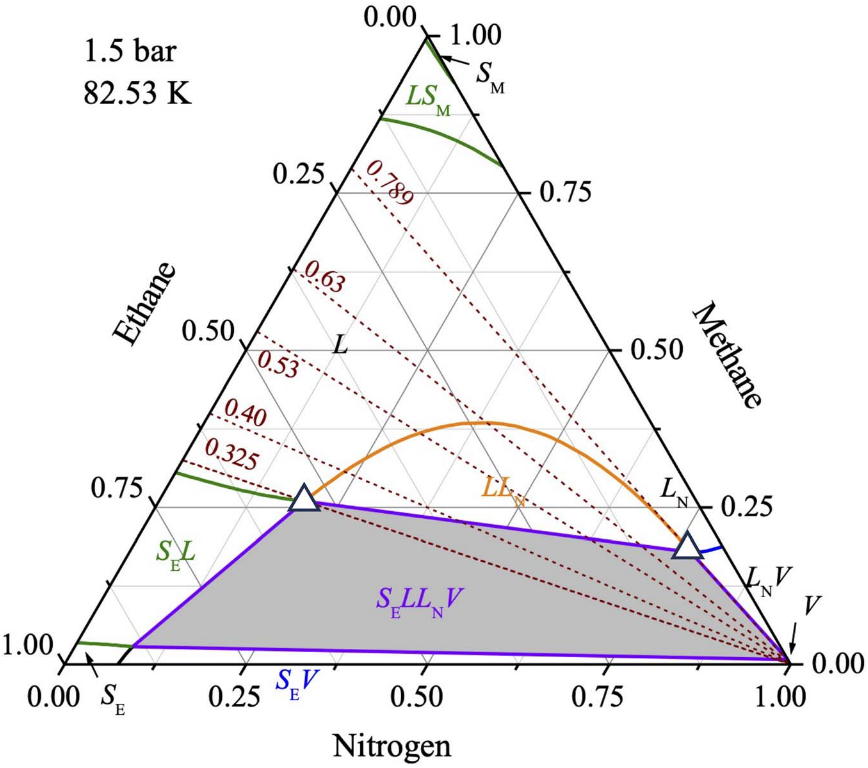

Figure 13. Calculated four-phase S_ELL_NV equilibrium of the CH_4–C_2H_6 +N_2 system. The four-phase temperature is 82.53 K at 1.5 bar and in the range 0.325–0.789 r_M, as denoted by the white triangles.

However, the phenomenon was a result of warming the sample and not a consequence of freezing.

We determined that the N_2 exsolution induced by ice formation only occurred in the S_ELV region of the pseudobinary phase diagram (Figure 4). Further, the cryodomes (Figure 11) were only seen in C_2H_6 +N_2 mixtures. Here we propose connections between surface phenomena and the by-products of freezing-induced exsolution. Specifically, we consider surface brightening after rainfall events (Section 4.1.1) and the possible consequences for cryomineral formation (Section 4.1.2).

4.1.1. Surface Brightening Post-rainfall

Cassini observations verified the presence of storms on Titan (Tomasko et al. 2005; Schaller et al. 2009; Turtle et al. 2011a) and their connections to temporal surface brightening events in at least four equatorial regions (Turtle et al. 2011c; Barnes et al. 2013). Analysis of ISS and VIMS data indicated a pattern of regional darkening at 0.938, 1.08, 1.28, 1.6, 2.0, 2.7, 2.8, and 5.0 μm wavelengths. The dimming lasted for weeks to months depending on location, then brightened beyond the pre-rainfall state, and finally relaxed back to the original brightness over a period of months. While the darkening was clearly linked to large cloudbursts, the source of the brightening and fading periods has been uncertain.

After further investigation, Barnes et al. (2013) proposed that the increased albedo may be the result of a transient layer of material, possibly a volatile, and not likely to be attributable to chemical alterations (e.g., rain washing the surface clean, sediment deposition, overturn, chemical weathering). One of the suggested scenarios was freezing due to evaporative cooling. Essentially, evaporation would continually cool and wick away moisture from the surface, leading to temperatures dipping below the freezing point and prompting ice formation. The ice would then either sublimate away or erode over time, explaining the relaxation phase. The proposed sequence may be conducive to exsolution-induced surface roughening. However, cryodome formation would necessitate rain reservoirs composed of C_2H_6-rich, N_2-poor liquid and surface temperatures around 88.5–89.9 K. As explained in Section 3.2.1, some amount of surface texturing may appear with the inclusion of CH_4 in the liquid, but this would also equate to depressed freezing point temperatures. Since raindrops are likely to be a combination of all three species, there must be a way for the CH_4 to disperse while simultaneously preserving some quantity of N_2.

A possible scenario may be liquid dissipation through a combination of evaporation and infiltration. With both mechanisms at play, the majority of C_2H_6 would remain as liquid on the surface, while the volatility of CH_4 and N_2 would lead to higher evaporation rates of the two (Graves et al. 2008; Dalba et al. 2012), and seepage into subsurface reservoirs would further deplete the CH_4 content (Hayes et al. 2018; Turtle et al. 2018; Faulk et al. 2020). To add to this, a study by Singh et al. (2017a) suggests that mixtures of CH_4 and N_2 can initiate evaporative cooling and may therefore provide a means of decreasing the surface temperature. If CH_4 dissipation were to outpace that of N_2 and evaporative cooling were able to sufficiently lower the surface temperature, this might result in a C_2H_6-enriched C_2H_6–N_2 mixture solidifying. Thus, N_2 would be trapped as the material froze and would then percolate through the C_2H_6-rich slurry, forming cryodomes as it escapes. This would equate to an increase in reflectivity due to the newly textured surface and would indicate the presence of C_2H_6 ice in IR spectra.

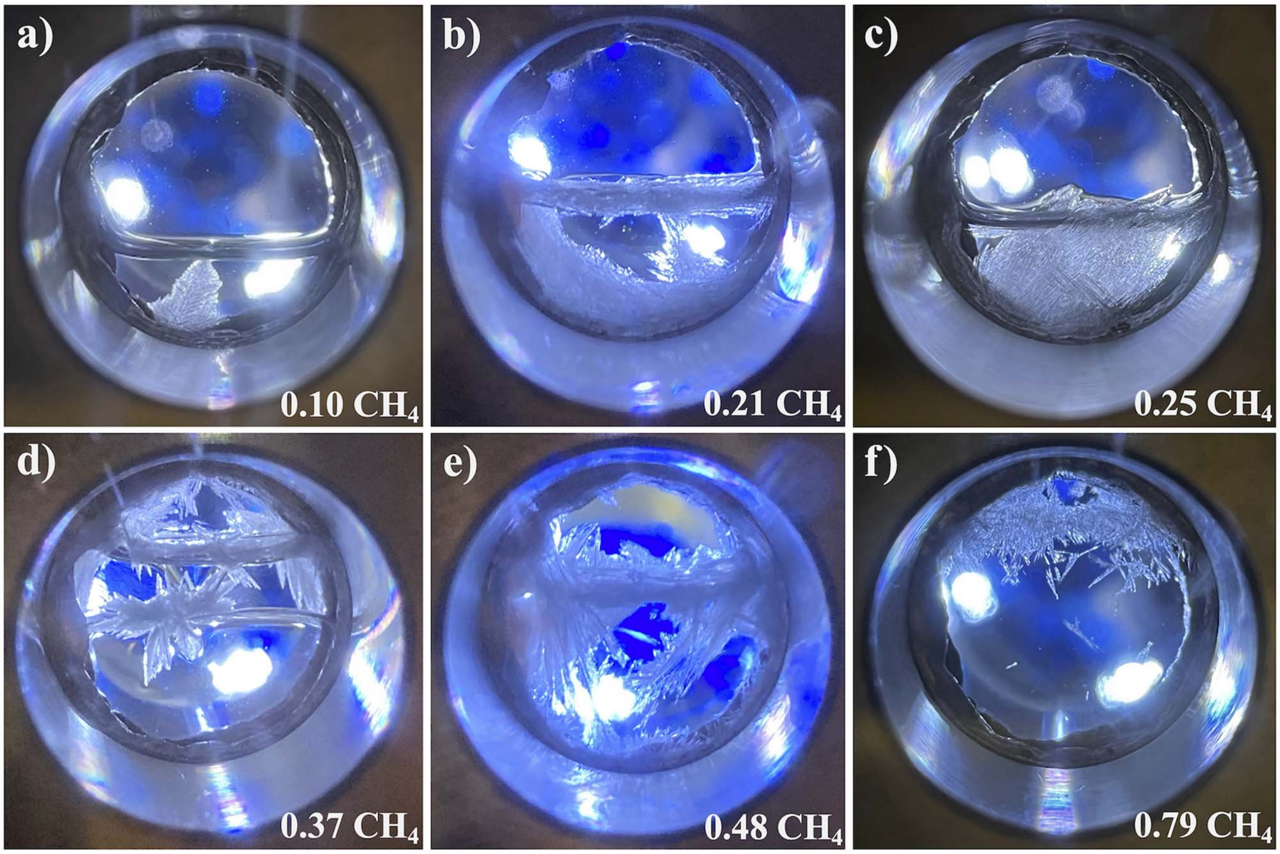

Figure 14. Examples of ice morphology in select CH_4 alkane ratios. Panels (a)–(c) depict ice morphologies characteristic of the S_ELV region, panel (d) is representative of ice in the S_ELL_NV region, and panels (e)–(f) show the ice morphology in samples that have passed the four-phase region and entered the $S_E$$L_N$V equilibrium.

In addition to cooling-only experiments, we also conducted annealing experiments that showed a decrease in cryodome formation and an increase in residing liquid with each cooling sequence (Figure 15). On Titan, this could translate to melting followed by partial reforming of ice upon cooling, consequently mottling the surface and decreasing the overall reflectivity of the region. Additionally, the remaining liquid would be susceptible to further evaporation and infiltration, meaning that the material would continue to dissipate and the affected area would eventually settle back to its original albedo. This process would only need a surface temperature fluctuation of ∼1–2 K to occur, assuming a C_2H_6–N_2 mixture. Unfortunately, temperature variability cannot be fully verified through Cassini data since no observations exist that can estimate surface temperatures during these post-rainfall events (Barnes et al. 2013).

Since our lab is not designed to operate on the timescale at which the surface dimming reportedly occurred, we can only comment on the appearance of the cryodomes and cannot attest to any long-term degradation processes. Thus, it would be advantageous to continue this study either through modeling or by utilizing a facility that can perform experiments continuously for months at a time.

4.1.2. Possible Consequences for Cryomineral Formation

Ethane has been observed in the atmosphere, on the surface, and is also projected to be part of Titan's subsurface processes. Consequently, it has become an important part of experimental cryomineral studies, especially for co-crystals (McConville et al. 2020; Cable et al. 2021; Czaplinski et al. 2023), evaporites (Malaska & Hodyss 2014; Singh et al. 2017b; Czaplinski et al. 2019), and clathrate hydrates (Vu et al. 2020). It has been a choice solvent in these experiments, and our results suggest that integrating N_2 into cryomineral studies may be a worthwhile endeavor, especially since the C_2H_6 liquid only needs to contain ∼0.08 N_2 mole fraction to prompt the exsolution process when freezing according to our experiments. This would inform us on the propensity for freezing-induced N_2 exsolution with additional solid species and whether peak formation can still occur. Any changes to surface roughness or spectral features could lead to insights on cryominerals formed in C_2H_6-rich environments and the roles they play in C_2H_6 sequestration and evaporative surface processes.

In the case of co-crystals, studies have shown that solvent choice can impact the co-crystal stoichiometric ratio, temperature of phase nucleation, and kinetics of formation (Leyssens et al. 2012; Hu et al. 2014; Saikia et al. 2021). Bora et al. (2023) also reported relative humidity having an influence on the formation and structure of a co-crystal, which is in part an attribute of the solvent composition. This can lead to changes in physiochemical properties like solubility, dissolution rate, and stability and extends to alterations in texture and spectral properties.

Adding N_2 to the C_2H_6 solvent would also be a sensible next step in that it more closely mimics the Titan liquid environment and would be particularly relevant in studies concerning the benzene:ethane (C_6H_6:C_2H_6) co-crystal. Cable et al. (2014) and

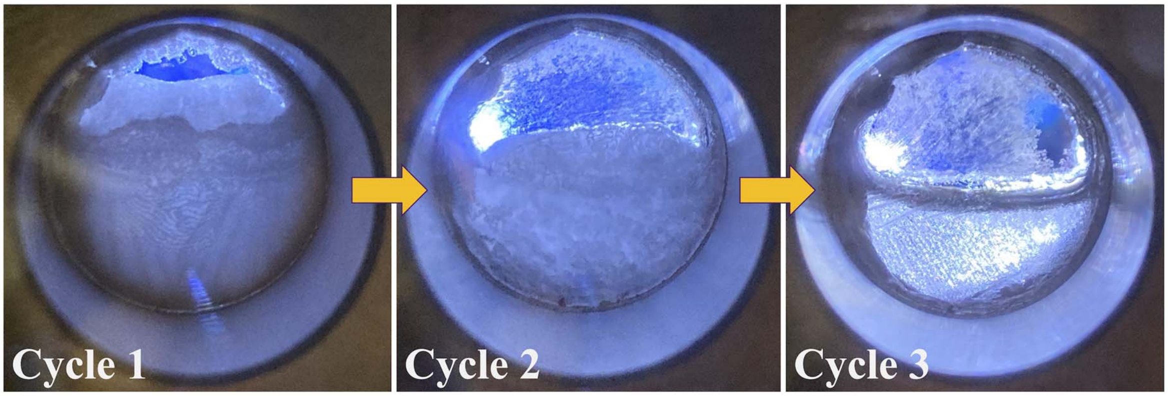

Figure 15. Changes in sample surface texture during an annealing experiment. The process consisted of cooling until freezing, warming to 95 K to melt the sample, and repeating for three rounds. Cycle 1 expanded and formed cryodomes; Cycle 2 took on the expanded/flat morphology and retained a small quantity of liquid; Cycle 3 showed almost no sign of surface roughening and remained mostly liquid.

Vu et al. (2014) showed that the C_6H_6:C_2H_6 co-crystal could form when a combination of solid benzene and liquid ethane was warmed, allowing the ethane to evaporate and leave an evaporitic deposit. Maynard-Casely et al. (2016) determined the stoichiometric ratio to be 3:1 C_6H_6:C_2H_6 when cycling the temperature between 90 and 130 K; however, it was posited that the trigonal space group might allow for 1:1 and 2:1 C_6H_6:C_2H_6 structures. That being said, it would be of use to identify whether the C_6H_6:C_2H_6 co-crystal can form in an C_2H_6–N_2 liquid and whether the stoichiometric ratio is affected. As a consequence, this may constrain, or perhaps broaden, the conditions that are needed to form the co-crystal. While the C_6H_6:C_2H_6 combination is the only C_2H_6-based co-crystal that has been studied in the lab thus far, many other structures have been created using C_2H_6 as the solvent (see Cable et al. 2021).

Molecular solid evaporites—those composed of a single species or a nonstoichiometric combination—are also an important consideration. Acetylene (C_2H_2), ethylene (C_2H_4), cyanoacetylene (HC_3N), and butane (C_4H_{10}) are a few species of interest for evaporite deposits (Clark et al. 2010; Cordier et al. 2013; Singh et al. 2017b; Czaplinski et al. 2019), in part due to their low evaporation rates and degrees of solubility. As with co-crystals, a change in solvent for the evaporites may affect the kinetics, temperatures of phase nucleation, and physiochemical properties, altering the formation processes on Titan and perhaps inducing co-crystal formation.

Vu et al. (2020) conducted experiments with liquid ethane and water ice to determine the feasibility of ethane clathrates forming at Titan surface conditions. The study not only confirmed clathrate formation but also indicated that they may be the dominant by-product in instances of liquid ethane pooling onto water ice. Additionally, ethane overlaying water ice may occur on Titan, as some studies suggest the presence of ethane in rainfall (Graves et al. 2008; Dalba et al. 2012) and the existence of exposed water-rich bedrock across Titan's equatorial region (Griffith et al. 2019). Generally, Vu et al. (2020) found that C_2H_6 clathrates formed more readily at higher temperatures, although they were still likely to form in <10 Earth years at 90 K. Since N_2 dissolution decreases with increasing temperature, it may have little to no effect on clathrate formation in the 150–173 K range used in the study. We have seen in the Astrophysical Materials Lab that small quantities of N_2 do remain in the liquid C_2H_6 at ambient surface temperatures (89–95 K), meaning that the altered solvent could still produce a different outcome, although the effects may not be producible on laboratory timescales.

While investigating the potential changes in cryomineral behavior is a vital facet to understanding Titan surface processes, we also need to determine how the introduction of a new species affects the exsolution-associated features. It would be of particular interest to define how the chemical environment informs the exsolution-induced surface roughening, e.g., if an C_2H_6–N_2 liquid were to infiltrate into an area of small grain water bedrock, would this prompt ethane clathrate formation upon freezing? Given the favorability of ethane as the guest molecule, low nitrogen retainment, and the immiscibility of nitrogen in both ethane and water, the interaction may result in nitrogen percolating out and pushing the icy material upward while doing so. The unique formation process may then be apparent in Cassini data, due to surface roughening and probable shifts in spectral features.

4.2. Air–Sea Interactions

Simulations created by Rafkin & Soto (2020) indicate that the most important conditions for ice formation are the presence of shallow mixed layers, low atmospheric humidity, and non-zero background wind. At appropriate initial conditions, the attributes could foster CH_4 evaporation that may cool the lakes to as low as 84 K—temperatures where lakes can permanently stratify into a CH_4-rich lower layer and C_2H_6-rich upper layer (Steckloff et al. 2020). Stratification may be occurring on present-day Titan, perhaps in the larger northern lakes as a shallow, cooler surface layer, due to nonideal liquid behavior that is defined by a decrease in density as the liquid cools (Tan et al. 2015). However, while it may be possible for lake conditions to reach these evaporative scenarios, it is unlikely that large-scale ice formations are in the lakes of present-day Titan since there have been no observed confirmations of significant ice structures to date.

A study by Steckloff et al. (2020) suggests that any C_2H_6-rich ice that precipitates out of liquid solution above ∼83 K will be denser and thus settle to the bottom of the lake. While conditions would necessitate lower-than-expected temperatures and high C_2H_6 levels for the process to occur, our results indicate that as the C_2H_6 ice forms and sinks, N_2 may be mostly or fully released from the solid, possibly giving rise to magic islands (Hofgartner et al. 2014, 2016) through the proposed mechanism of nitrogen bubbles (Cordier et al. 2017; Hanley 2017; Malaska et al. 2017; Farnsworth et al. 2019).

Alternatively, it is conceivable for ice to form at a small scale, particularly along shorelines. This is of interest given previous studies speculating that precipitation and evaporation processes from cool moist ground might contribute to a delay in temperature rise during transitions between northern winter and spring (Jennings et al. 2016). Assuming a C_2H_6-rich dampened surface (Williams et al. 2012) and a temperature of 89 K down to 84 K, our results suggest that ice could plausibly precipitate out of solution, assuming that the liquid reached a composition of 0.05–0.25 r_M (Figure 4). These conditions might be reached during polar nights and would therefore allow for ice to be a typical marine microclimate feature (Rafkin & Soto 2020). In addition, while studies have reported wind speeds of roughly 0.2–0.3 m s^{-1} (Lorenz 2006; Tokano 2009; Tokano & Lorenz 2016), there may be circumstances in which higher winds could be produced and thus contribute to a conducive environment for ice. Topography, irregular shorelines, interference between sea breezes, and the potential for cyclone formation can locally accelerate winds (Tokano 2013; Chatain et al. 2022), which would be of great importance in the case of ice formation around lakes. Of course, other small liquid reservoirs may provide similar conditions appropriate for ice formation to those seen on shorelines, although the aspects that could allow for stronger background winds are likely not present.

4.3. Paleoclimate

Titan is currently losing its atmospheric CH_4, due to photoionization in the upper atmosphere (Niemann et al. 2005; Waite et al. 2005); in ∼50–100 Myr, Titan is expected to lose sufficient CH_4 to shut down its N_2 greenhouse effect and cool by ∼10 K (Lorenz et al. 1997). Under these snowball Titan conditions—also referred to as a "slushball" Titan (Battaglia 2020; Steckloff et al. 2021)—any released CH_4 would preferentially dissolve in Titan's surface liquids, rather than remain in the atmosphere (Steckloff et al. 2020). This process is likely cyclical, with Titan's climate proposed to cycle between the current warm Titan and slushball Titan (Steckloff et al. 2020), although the timescales and equilibrium surface conditions under these different regimes are currently poorly understood. The colder temperatures of a slushball Titan state heighten the possibility of multiphase equilibria at the surface of the lakes. Under these conditions, significant amounts of solid materials may precipitate out of solution and either settle to the lakebed or float to the surface; the latter case would hamper material exchange between the surface liquids and atmosphere (sequestering the hydrocarbons in the lake) and may produce bright ice that further reflects light and cools the surface. In other words, the complicated behavior of the freezing point trend in the CH_4–C_2H_6–N_2 system under Titan-like conditions could further stabilize the slushball Titan state. However, the slushball Titan would be accompanied by a reduced atmospheric pressure, due to the partial collapse of Titan's atmosphere (Lorenz et al. 1997; Charnay et al. 2014). The atmospheric pressure may drop to ∼0.7 bars (Lorenz et al. 1997; Charnay et al. 2014), complicating the application of this work to the surface of slushball Titan's lakes. Nevertheless, the hydrostatic pressure of the lakes at some depth below the surface would reach 1.5 bars, where the results in the present study would still hold. Therefore, the results of the experiments and CRYOCHEM 2.0 model could inform future paleoclimate modeling endeavors.

5. Conclusions and Remarks

Our experiments and calculations indicate that N_2 depresses or flattens the freezing point temperature profile of the CH_4–C_2H_6 binary system depending on the CH_4 N_2-free mole fraction, r_M. At <0.32 ± 0.03 r_M experimentally and <0.325 r_M computationally, the freezing point trend follows the binary liquidus and crosses a solid–liquid–vapor (S_ELV, where the subscripted "E" represents an ethane-rich phase) boundary at the first appearance of ice. This portion of the pseudo-binary phase diagram also exhibits N_2-rich exsolution in tandem with the first appearance of ice, and the degree of exsolution increases with decreasing r_M. In mixtures between 0.32 ± 0.03 r_M and 0.79 ± 0.03 r_M experimentally and 0.325–0.789 r_M computationally, the system arrives at a solid–liquid–liquid–vapor (S_ELL_NV, where the subscripted "N" signifies a nitrogen-rich phase) boundary with first ice at 82.3 ± 0.3 K and 82.53 K, respectively. During experiments, samples corresponding to this r_M range would enter an LL_NV equilibrium at ∼83 K and then pass through the S_ELL_NV boundary while cooling to temperatures below 82.53 K. The sequence of phase transitions results in an isothermal freezing point profile that ceased once CH_4 content surpassed ∼0.8 r_M. From here, freezing points could not be recorded, due to the absence of a solid phase upon isobaric cooling at 1.5 bars while traveling along the $+N_2$ cooling path.

We also found the ice morphology to share similar characteristics depending on whether the sample crossed the S_ELV or S_ELL_NV boundary while traveling along the $+N_2$ cooling path (Figure 14). At S_ELV equilibrium, ice generally formed at or near the bottom of the cell and took on a more "feathery" appearance. The structure became more tenuous with increasing CH_4 composition, likely because more N_2 was able to remain in the liquid phase. Conversely, ice that formed in samples that fell in the S_ELL_NV region of the pseudo-binary phase diagram (Figure 4) had a "spiky" quality—similar to the morphology of the ice that formed along the C_2H_6 branch of the CH_4–C_2H_6 binary system (Engle et al. 2021)—forming in the hydrocarbon-rich top layer, starting at the LL_N interface and expanding further into the top layer.

In addition to mapping the freezing points, we also recorded the amount of N_2 dissolution into the LV equilibrium while cooling isobarically from 95 K to as low as 82.5 K, with the lower limit being dependent on the temperature at which ice or a second liquid formed. As expected, we found that N_2 dissolution increased with decreasing temperature and increasing r_M. The effects of pressure on N_2 solubility were not directly considered here, given our focus on the behaviors of the system under isobaric conditions. However, previous studies have shown that N_2 dissolution increases with increasing pressure (Cordier et al. 2017; Malaska et al. 2017; Hartwig et al. 2018; Richardson et al. 2018) and that even relatively small changes in the pressure can have a noticeable impact on the locations of phase boundaries in the ternary system (Tan & Kargel 2018). While outside the scope of this project, future studies should consider investigating the sensitivity of the CH_4–C_2H_6–N_2 system to changes in pressure and how it might apply to processes occurring in Titan's atmosphere and at depth in the seas.

In all, the intent of the work presented here was to monitor the effects of N_2 on the CH_4–C_2H_6 system under current Titan surface conditions (1.5-bar N_2 pressure), specifically with regard to multiphase equilibria and phase transitions. Although adding N_2 to the alkane system did not strongly indicate freezing at the surface conditions documented during the Cassini mission, small-scale environmental changes may allow for ice and liquid to coexist. Examples of these environments include shallow ponds, C_2H_6-rich rain puddles, receding lakes, along the shorelines of larger lakes, and possibly in an earlier time when Titan may have been a "slushball."

Acknowledgments

This work was sponsored by NASA FINESST Fellowship grant NNH19ZDA001N-FINESST, NASA SSW grant Nos. 80NSSC18K0203 and 80NSSC19K0556, NASA CDAP grant No. 80NSSC18K0967, the John and Maureen Hendricks Foundation, and the Lowell Observatory Slipher Society.

Data Availability

Data behind the figures presented in this work, along with other supporting materials, can be found at doi:10.6084/m9.figshare.c.7087474.

Appendix

A.1. Temperature Progression in the Isobaric Cooling of Ternary CH_4–C_2H_6–N_2 at 1.5 bars

In Figure A1(a), the left-hand side of the ternary diagram representing the binary methane–ethane is the same as the horizontal axis of the pseudo-binary phase diagram in Figure 4. The vertical axis in the pseudo-binary diagram is the temperature, which can be set up in Figure A1(a) to be perpendicular to the composition diagram out from the plane toward our eyes. The 3D isobaric phase diagram is generically shown in Figure A1(b), where every horizontal cross section is the composition diagram at a certain temperature. Therefore, Figure 4 is actually the projection of the 3D diagram onto the left-hand vertical hatched plane of the prism.

A.2. Thermodynamic Description on Detecting the Isobaric Freezing Point

In our experiments of detecting the freezing temperatures, the cooling starts at a temperature T_3 as illustrated in a typical composition diagram in Figure A2(a), where the pressurizing vapor is in equilibrium with a liquid phase; thus, the overall composition is in the LV region on the constant methane alkane ratio line, e.g., point A. As the temperature decreases to T_2, illustrated in Figure A2(b) by the corresponding three-phase SLV region, more N_2 is injected to maintain the constant pressure, which means that the overall composition shifts toward the pure N_2 vertex along the line. The exact location of the overall composition on the line depends on the total volume of the system, which determines how much N_2 will be added to maintain the constant pressure at T_2. In Figure A2(b), the new total composition is at point B, which is still in the LV region despite the upward shift of the three-phase SLV region. Finally, upon further cooling to T_1, more N_2 is injected to maintain the constant pressure, and the overall composition touches the SLV region, i.e., point C in Figure A2(b), where the first chunk of solid phase appears. This means that T_1 is the freezing temperature of the mixture, with the methane alkane ratio represented by the line.

In our experiments, the pressure is fixed, so that the freezing temperature is in principle readily measured if the composition is known. The composition dependence in the detection is the consequence of the phase rule, where three-phase equilibria for ternary mixtures are bivariant. However, it is worth noting that

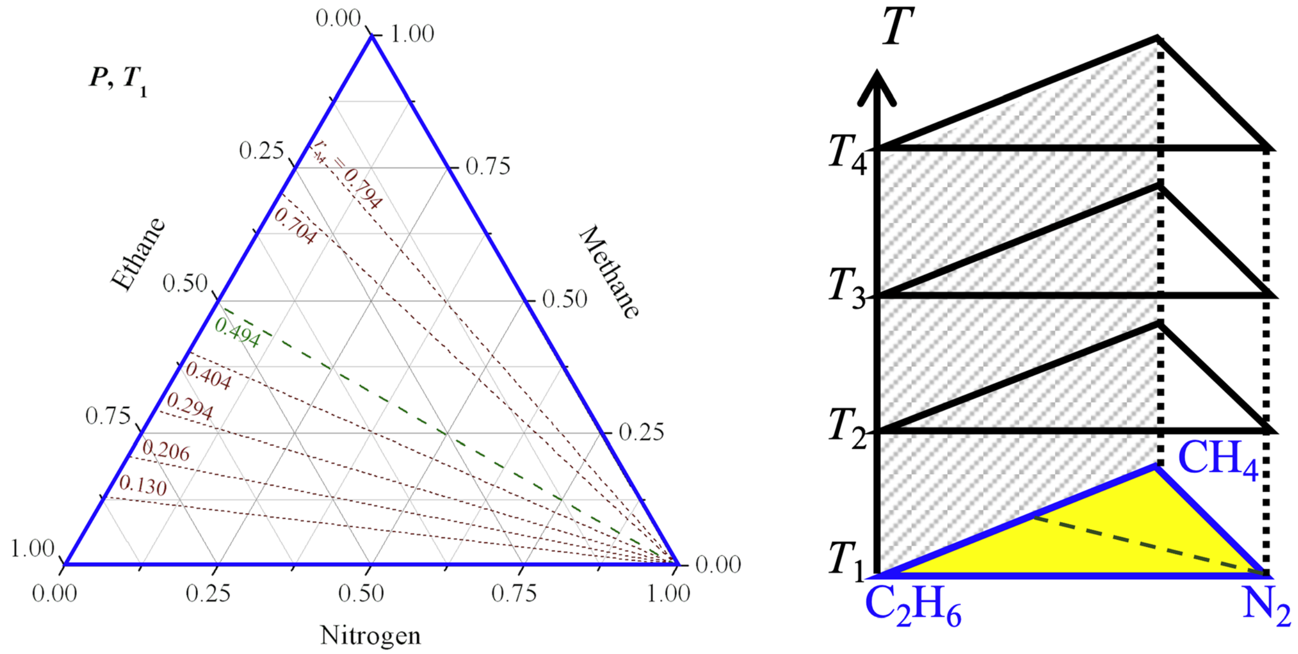

(a) **(b)**

Figure A1. Phase diagrams of ternary mixtures: relation between composition diagram (panel (a)) and the temperature–composition pseudo-binary diagram at constant pressure (hatched projection plane in panel (b)).

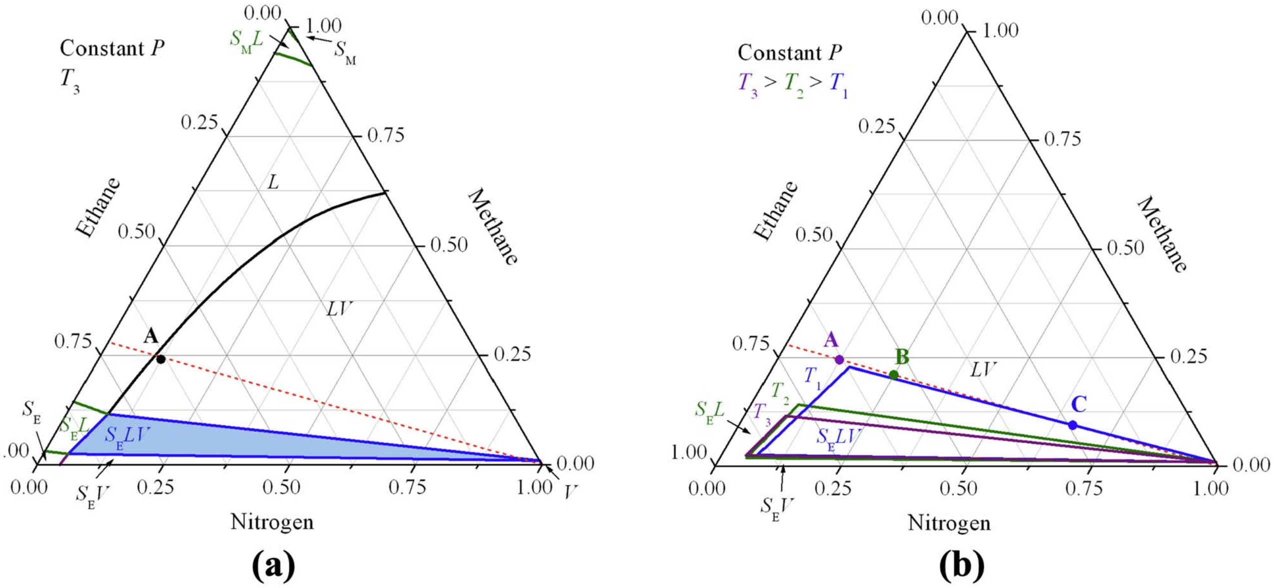

Figure A2. Typical composition phase diagrams: detection of the freezing temperature of a ternary mixture, with r_M represented by the dotted line at a constant pressure P. (a) The complete topography at T_3; cooling starts at A in the LV region. (b) SLV regions at $T_1 < T_2 < T_3$; as the cooling proceeds to T_2, where the total composition B is still in the LV region. Upon further cooling to T_1, the total composition C is on the LV side of the corresponding SLV region, where solid is the incipient phase, which indicates that T_1 is the freezing temperature.

Table A1
S_ELL_NV Equilibrium Compositions and Densities of N_2–CH_4–C_2H_6 System at 82.53 K and 1.5 bars

Equilibrium Phase	Equilibrium Compositions (mol frac)			Equilibrium Densities
	Nitrogen (N_2)	Methane (CH_4)	Ethane (C_2H_6)	(kg m^{-3})
Solid (S_E)	0.0797	0.0282	0.8921	729.51
Liquid 1 (L)	0.2002	0.2598	0.54	648.62
Liquid 2 (L_N)	0.7732	0.1789	0.0479	732.85
Vapor	0.9921	0.0079	6.00E–05	6.44

the temperature and the corresponding amount of N_2 to be injected to maintain the constant pressure can fluctuate. Therefore, the total composition varies despite using a constant methane nitrogen-free mole fraction, r_M, as discussed earlier. This fact may also cause overshooting in pressure and/or temperature, which introduces errors to the measurements. Overshooting the pressure from a lower value after cooling is a primary source of inaccuracy, because there is no way to maintain the constant r_M if correcting the pressure by bleeding some vapor out from the system. Although, as noted in Section 2.1, decreasing the pressure in the cell via material removal was generally avoided so as to lower the risk of unintentionally changing the methane alkane ratio. Visual detection and supercooling may also easily overshoot the freezing temperature to a lower value.

Although the r_M values are known during our experiments, there are no data for the total composition of the alkanes and nitrogen; thus, CRYOCHEM 2.0 estimates the freezing temperature to be that for the upper vertex of the S_ELV region, which is in fact the minimum freezing temperature of the mixture that has the corresponding r_M. If the total composition were at this vertex, the cell would contain just the liquid phase in equilibrium with both vapor and solid as the incipient phases. The EOS can also used to estimate the amount of N_2 that dissolves into the liquid along the cooling using the bubble-point curves as described in Sections 2.2 and 3.1.

A.3. Cooling: 89 K to 83 K

At about 89 K, the ethane-rich solid phase S_E has grown enough to introduce the three-phase S_ELV equilibrium (Figure A3(a)). At 87 K, the initial two-phase equilibrium LV from the start of cooling still occupies a wide range of compositions, as shown in Figure A3(b), while the S_ELV region widens. The region keeps growing at 85 K (Figure A3(c)) and at 83 K (Figure A3(d)), where a second liquid appears, as well as the accompanying three-phase LL_NV region that narrows the LV region. A small r_M of 0.29 passes through the S_ELV region at 83 K, meaning it must have passed its freezing point earlier at a higher temperature, which can also be evaluated from Figure 6. On the other hand, a values of 0.65 r_M passes through the LL_NV region, which means that there are two liquids observed in the experiment prior to the freezing temperature. Only after the LV gap is closed at the four-phase equilibrium at 82.53 K (Figure 9) does the first chunk of solid S_E appear and thus the freezing point. In Figure 6, after the cooling arrives at the LL_NV curve, it traces the curve toward the four-phase point F; for even higher r_M values, it traces the curve toward point G instead of F. Therefore, for high r_M values, the second liquid must appear first before the solid. On the contrary, for low r_M values, the solid appears at the freezing temperature on the S_ELV curve without observing the second liquid beforehand.

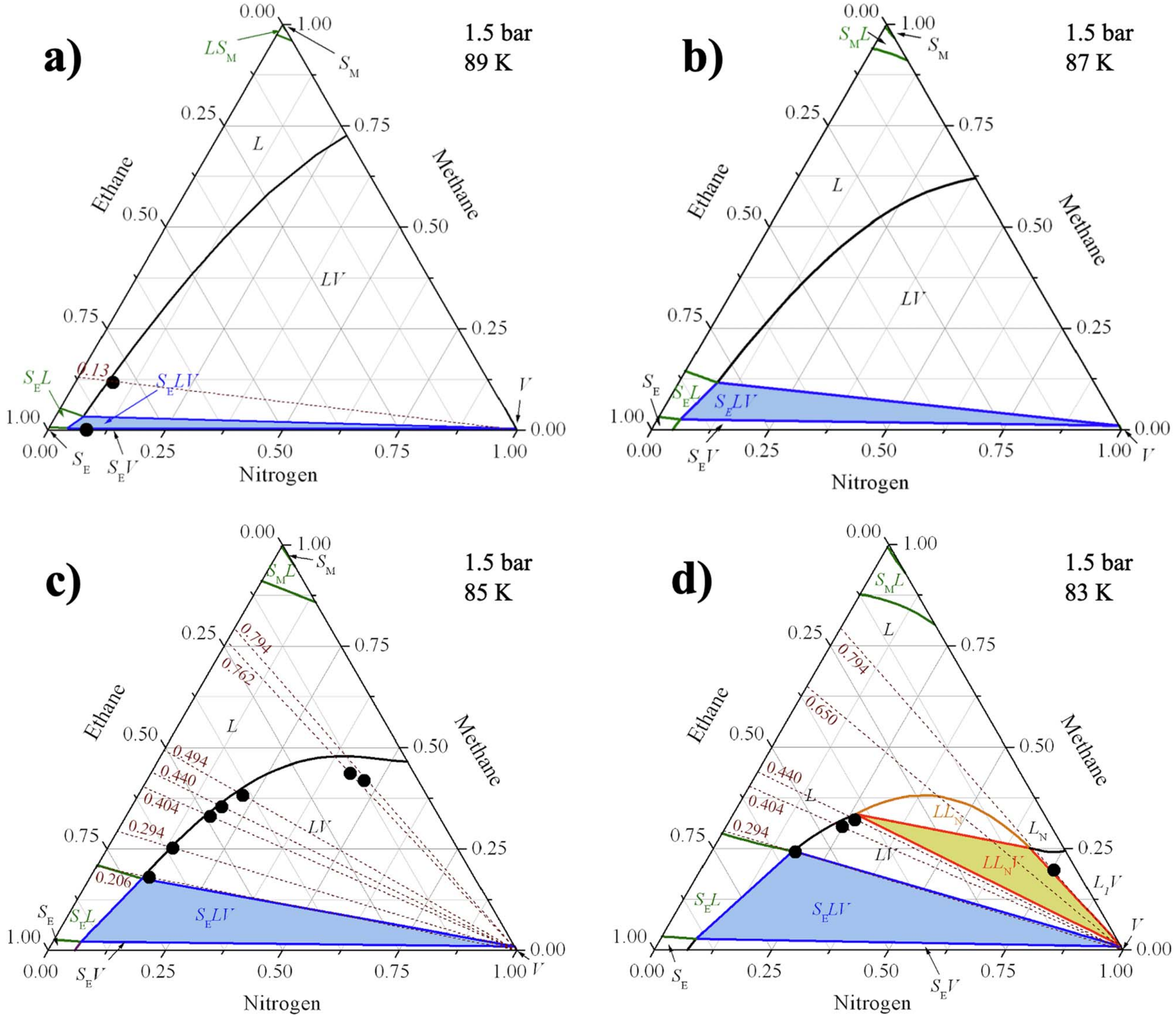

Figure A3. Cooling progression: (a) 89 K; (b) 87 K; (c) 85 K; (d) 83 K. Filled black circles are experimental N_2 dissolution data. The results for higher temperatures (95 K and 90 K) are provided in Figure 9.

Note that, as discussed earlier, the four-phase equilibrium for ternary mixtures is univariant. Therefore, as long as the pressure is 1.5 bars, regardless of the amount of N_2 needed to maintain the pressure, the $S_E L L_N V$ occurs at the same temperature, which is calculated to be at 82.53 K as shown in Figure 9 and at points F and G in Figure 6. Consequently, for 0.325–0.789 r_M, the pseudo-binary phase diagram observes a constant freezing temperature of 82.53 K in Figure 4. The equilibrium compositions and densities of the ternary mixture at the $S_E L L_N V$ equilibrium are listed in Table A1. As seen in the table, solid S_E has a density larger than liquid L but smaller than the N_2-rich liquid L_N.

A.4. Further Cooling to Lower Temperatures

Further cooling from the four-phase temperature splits the four-phase region into two three-phase regions, but with combinations different from that at higher temperatures. They are now $S_E L L_N$ and $S_E L_N V$ as shown in Figures A4(a)–(b), with $S_E L_N$ in the gap in between. The noticeable phase behavior at these low temperatures is that the vapor phase is disappearing, while the remaining equilibrium between vapor and liquid is $L_N V$, which also eventually disappears at about 80.9 K, i.e., the condensation point of pure N_2 at 1.5 bars. Below this temperature, only liquid and solid phases remain at this pressure. At even lower temperatures all three-phase regions disappear, leaving only two SL regions after $S_E L$ and $S_E L_N$ merge together into a continuous region, while the other region is $S_M L$.

As seen in Figure A4, mixtures beyond 0.789 r_M (e.g., 0.80 r_M) are in the $L_N V$ region in the presence of vapor. Since it crosses the $S_E L_N V$ region through the $L_N V$ side very close to pure N_2, the freezing temperature experimentally cannot be reached before overfilling the cell with liquid as N_2 is injected to maintain the pressure. In Figure 6, the $S_E L_N V$ curve is located at high N_2 mole fractions (green curve) from point G going up to pure N_2 (the condensation point of pure N_2 at 80.9 K at 1.5 bars).

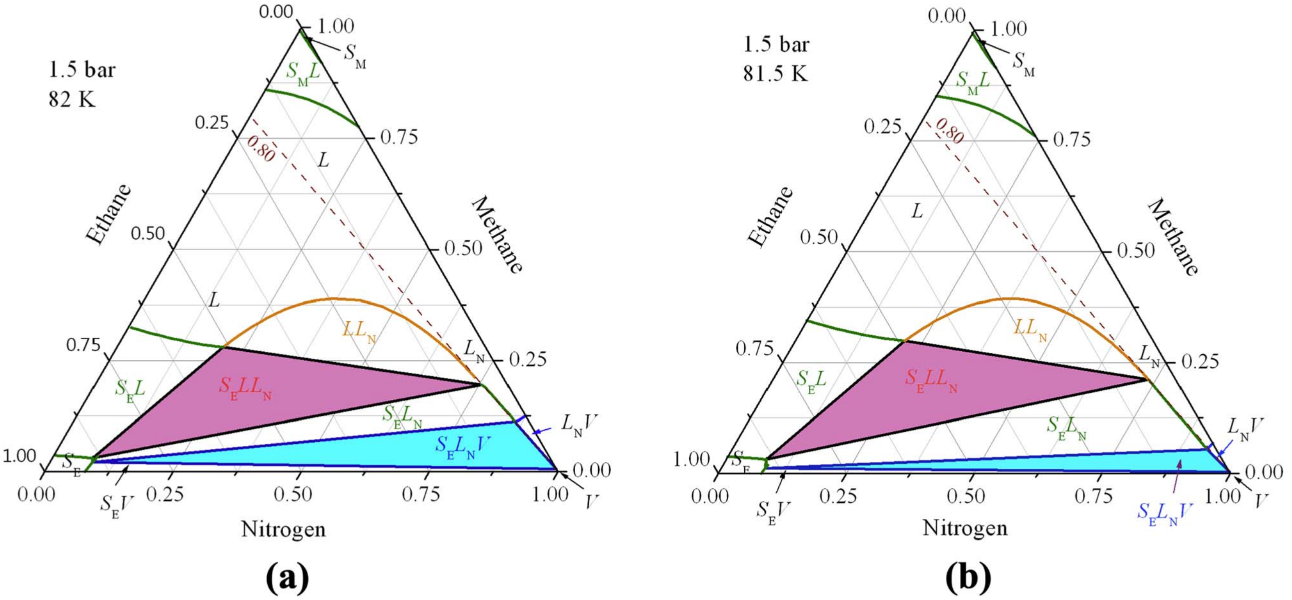

Figure A4. Cooling from (a) 82 K to (b) 81.5 K.

ORCID iDs

Anna E. Engle https://orcid.org/0000-0002-7894-7056
Jennifer Hanley https://orcid.org/0000-0002-0801-7654
Sugata P. Tan https://orcid.org/0000-0003-2049-3706
William M. Grundy https://orcid.org/0000-0002-8296-6540
Stephen C. Tegler https://orcid.org/0000-0002-6794-495X
Gerrick E. Lindberg https://orcid.org/0000-0002-5292-4200
Jordan K. Steckloff https://orcid.org/0000-0002-1717-2226
Shaelyn M. Raposa https://orcid.org/0000-0002-8691-5214
Cecilia L. Thieberger https://orcid.org/0000-0001-7399-434X
Shyanne Dustrud https://orcid.org/0000-0001-6758-2226
Jessica J. Groven https://orcid.org/0000-0002-1254-3606
Logan A. Pearce https://orcid.org/0000-0003-3904-7378

References

Barnes, J. W., Bow, J., Schwartz, J., et al. 2011, Icar, 216, 136
Barnes, J. W., Buratti, B. J., Turtle, E. P., et al. 2013, PlSci, 2, 1
Barnes, J. W., Sotin, C., Soderblom, J. M., et al. 2014, PlSci, 3, 3
Battaglia, S. M. 2020, LPSC, 51, 1118
Birch, S. P. D., Hayes, A. G., Corlies, P., et al. 2018, Icar, 310, 140
Bora, P., Pathak, D., Kalita, B. K., & Sarma, B. 2023, Cryst. Growth Des., 23, 1500
Bradley, M. S. 2015, Spectroscopy, 30, 42
Brown, R. H., Soderblom, L. A., Soderblom, J. M., et al. 2008, Natur, 454, 607
Buchsbaum, S., Mills, R. L., & Schiferl, D. 1984, JPhCh, 88, 252
Cable, M. L., Runčevski, T., Maynard-Casely, H. E., Vu, T. H., & Hodyss, R. 2021, Acc. Chem. Res., 54, 3050
Cable, M. L., Tuan, T. H., Hodyss, R., et al. 2014, GeoRL, 41, 5396
Charnay, B., Forget, F., Tobie, G., Sotin, C., & Wordsworth, R. 2014, Icar, 241, 269
Chatain, A., Rafkin, S. C. R., Soto, A., Hueso, R., & Spiga, A. 2022, PSJ, 3, 232
Clark, R. N., John, M. C., Barnes, J. W., et al. 2010, JGR, 115, E10005
Cordier, D., Barnes, J. W., & Ferreira, A. G. 2013, Icar, 226, 1431
Cordier, D., García-Sánchez, F., Justo-García, D. N., & Liger-Belair, G. 2017, NatAs, 1, 1
Cordier, D., & Liger-Belair, G. 2018, ApJ, 859, 26
Czaplinski, E. C., Gilbertson, W. A., Farnsworth, K. K., & Chevrier, V. F. 2019, ESC, 3, 2353
Czaplinski, E. C., Vu, T. H., Morgan, M. L., et al. 2023, ESC, 7, 597
Dalba, P. A., Buratti, B. J., Brown, R. H., et al. 2012, ApJL, 761, L24
Engle, A. E., Hanley, J., Dustrud, S., et al. 2021, PSJ, 2, 118
Farnsworth, K. K., Soto, A., Chevrier, V. F., Steckloff, J. K., & Soderblom, J. M. 2023, ESC, 7, 439
Farnsworth, K. K., Vincent, F. C., Steckloff, J. K., et al. 2019, GeoRL, 46, 13658
Faulk, S., Lora, J., Lora, J., Mitchell, J. L., & Milly, P. 2020, NatAs, 4, 390
Glein, C. R., & Shock, E. L. 2013, GeCoA, 115, 217
Graves, S. D. B., McKay, C. P., Griffith, C. A., Ferri, F., & Fulchignoni, M. 2008, P&SS, 56, 346
Griffith, C. A., Penteado, P. F., Turner, J. D., et al. 2019, NatAs, 3, 642
Grundy, W. M., Morrison, S. J., Bovyn, M. J., Tegler, S. C., & Cornelison, D. M. 2011, Icar, 212, 941
Hanley, J. 2017, NatAs, 1, 0122
Hartwig, J., Meyerhofer, P., Lorenz, R., & Lemmon, E. 2018, Icar, 299, 175
Hayes, A., Aharonson, O., Callahan, P., et al. 2008, GeoRL, 35, L09204
Hayes, A. G., Aharonson, O., Lunine, J. I., et al. 2011, Icar, 211, 655
Hayes, A. G., Lorenz, R., & Lunine, J. I. 2018, NatGe, 11, 306
Hofgartner, J. D., Hayes, A. G., Lunine, J. I., et al. 2014, NatGe, 7, 493
Hofgartner, J. D., Hayes, A. G., Lunine, J. I., et al. 2016, Icar, 271, 338
Hofgartner, J. D., & Lunine, J. I. 2013, Icar, 223, 628
Hörst, S. M. 2017, JGRE, 122, 432
Hu, P., Ma, L., Tan, K. J., et al. 2014, Cryst. Growth Des., 14, 6376
Jennings, D. E., Cottini, V., Nixon, C. A., et al. 2016, ApJL, 816, L17
Korppi-Tommola, J., Sundius, T., Shurvell, H. F., & Daunt, S. J. 1990, JRSp, 21, 255
Kumar, P., & Chevrier, V. F. 2020, ESC, 4, 241
Le Gall, A., Malaska, M. J., Lorenz, R. D., et al. 2016, JGRE, 121, 233
Leyssens, L., Springuel, G., Montis, R., Candoni, N., & Veesler, S. 2012, Cryst. Growth Des., 12, 1520
Lopes, R. M. C., Stofan, E. R., Peckyno, R., et al. 2010, Icar, 205, 540
Lopes, R. M. C., Wall, S. D., Elachi, C., et al. 2019, SSRv, 215, 33
Lora, J. M., Battalio, J. M., Yap, M., & Baciocco, C. 2022, Icar, 384, 115095
Lorenz, R. 2006, Icar, 182, 559
Lorenz, R., Rosaly, M. L., Paganelli, F., et al. 2008, P&SS, 56, 1132
Lorenz, R. D. 2021, JGRE, 126, e06786
Lorenz, R. D., McKay, C. P., & Lunine, J. I. 1997, Sci, 275, 642
Lunine, J. I., & Atreya, S. K. 2008, NatGe, 1, 159
MacKenzie, S. M., & Barnes, J. W. 2016, ApJ, 821, 17
MacKenzie, S. M., Barnes, J. W., Hofgartner, J. D., et al. 2019, NatAs, 3, 506
Malaska, M., Radebaugh, J., Mitchell, K., et al. 2011, in First Int. Planetary Caves Workshop: Implications for Astrobiology, Climate, Detection, and Exploration, 15
Malaska, M. J., Ashley Schoenfeld, J. J., Wynne, K. L., et al. 2022, JGRE, 127, e2022JE007512
Malaska, M. J., & Hodyss, R. 2014, Icar, 242, 74
Malaska, M. J., Hodyss, R., Lunine, J. I., et al. 2017, Icar, 289, 94
Malaska, M. J., Radebaugh, J., Lopes, R. M. C., et al. 2020, Icar, 344, 113764

Mastrogiuseppe, M., Hayes, A. G., Poggiali, V., et al. 2018, Icar, 300, 203
Mastrogiuseppe, M., Poggiali, V., & Hayes, A. G. 2019, NatAs, 3, 535
Maynard-Casely, H. E., Hodyss, R., Cable, M. L., Vu, T. H., & Rahm, M. 2016, IUCrJ, 3, 192
McConville, C. A., Tao, Y., Evans, H. A., et al. 2020, Chem. Commun., 56, 13520
Niemann, H. B., Atreya, S. K., Bauer, S. J., et al. 2005, Natur, 438, 779
Pelletier, M. J. 2003, ApSpe, 57, 20A
Poggiali, V., Mastrogiuseppe, M., Hayes, A. G., et al. 2016, GeoRL, 43, 7887
Radebaugh, J., Ventra, D., Lorenz, R. D., et al. 2018, GSLSP, 440, 281
Rafkin, S. C. R., & Soto, A. 2020, Icar, 351, 113903
Raposa, S. M., Sugata, P. T., Grundy, W. M., et al. 2022, JChPh, 157, 064201
Raposa, S. M., Tan, S. P., Grundy, W. M., et al. 2024, PSJ, submitted
Richardson, I. A., Hartwig, J. W., & Leachman, J. W. 2018, Fluid Phase Equilib., 462, 38
Richardson, I. A., Hartwig, J. W., & Leachman, J. W. 2019, IJTS, 137, 534
Saikia, B., Pathak, D., & Sarma, B. 2021, CrystEngComm, 23, 4583
Schaller, E. L., Roe, H. G., Schneider, T., & Brown, M. E. 2009, Natur, 460, 873
Shimanouchi, T. 1972, JPCRD, 1, 189
Singh, G., Singh, S., Wagner, A., et al. 2017a, Ap&SS, 362, 184
Singh, S., Combe, J.-Ph., Cordier, D., et al. 2017b, GeCoA, 208, 86
Solomonidou, A., Le Gall, A., Malaska, M. J., et al. 2020, Icar, 344, 113338
Steckloff, J. K., Soderblom, J. M., Farnsworth, K. K., et al. 2020, PSJ, 1, 26
Steckloff, J. K., Soderblom, J. M., & Soto, A. 2021, LPSC, 52, 1036
Stofan, E. R., Elachi, C., Lunine, J. I., et al. 2007, Natur, 445, 61
Tan, S. P., Adidharma, H., Kargel, J. S., & Marion, G. M. 2013, FlPEq, 360, 320
Tan, S. P., & Kargel, J. S. 2018, FlPEq, 458, 153
Tan, S. P., Kargel, J. S., Jennings, D. E., et al. 2015, Icar, 250, 64
Tegler, S. C., Stufflebeam, T. D., Grundy, W. M., et al. 2019, AJ, 158, 17
Tokano, T. 2009, Icar, 204, 619
Tokano, T. 2013, Icar, 223, 766
Tokano, T., & Lorenz, R. 2016, Icar, 270, 67
Tomasko, M. G., Archinal, B., Becker, T., et al. 2005, Natur, 438, 765
Turtle, E. P., Del Genio, A. D., Barbara, J. M., et al. 2011a, GeoRL, 38, L03203
Turtle, E. P., Perry, J. E., Barbara, J. M., et al. 2018, GeoRL, 45, 5320
Turtle, E. P., Perry, J. E., Hayes, A. G., & McEwen, A. S. 2011b, Icar, 212, 957
Turtle, E. P., Perry, J. E., Hayes, A. G., et al. 2011c, Sci, 331, 1414
Vu, T. H., Cable, M. L., Choukroun, M., Hodyss, R., & Beauchamp, P. 2014, JPCA, 118, 4087
Vu, T. H., Choukroun, M., Sotin, C., Muñoz-Iglesias, V., & Maynard-Casely, H. E. 2020, GeoRL, 47, e86265
Waite, J. H., Jr., Niemann, H., Yelle, R. V., et al. 2005, Sci, 308, 982
Williams, K. E., McKay, C. P., & Persson, F. 2012, P&SS, 60, 376
Wisnosky, M. G., Eggers, D. F., Fredrickson, L. R., & Decius, J. C. 1983, JChPh, 79, 3505
Wynne, J. J., Mylroie, J. E., Titus, T. N., et al. 2022, JGRE, 127, e2022JE007303